Projection studies of Higgs boson pair production to the 4 b-jet final state at the HL-LHC using the ATLAS detector

by

Colm Sam

A THESIS SUBMITTED IN PARTIAL FULFILLMENT OF
THE REQUIREMENTS FOR THE DEGREE OF

MASTER OF SCIENCE

in

The Faculty of Graduate and Postdoctoral Studies

(Physics)

THE UNIVERSITY OF BRITISH COLUMBIA

(Vancouver)

March 2023

The following individuals certify that they have read, and recommend to the Faculty of Graduate and Postdoctoral Studies for acceptance, the thesis entitled:

Projection studies of Higgs boson pair production to the 4 b-jet final state at the HL-LHC using the ATLAS detector

submitted by **Colm Sam** in partial fulfillment of the requirements for the degree of **Master of Science** in **Physics**.

Examining Committee:

Alison Lister, Associate Professor, Physics & Astronomy, UBC
Co-Supervisor

Maximilian Swiatlowski, Associate Research Scientist, TRIUMF
Co-Supervisor

Scott Oser, Professor, Physics & Astronomy, UBC
Supervisory Committee Member

Abstract

Projection studies for the non-resonant Higgs boson pair production in the $b\bar{b}b\bar{b}$ final state with the ATLAS detector at the HL-LHC are presented. They are based on extrapolated results of the latest Run 2 analysis which targeted both the gluon-gluon fusion and vector-boson fusion Higgs boson pair production modes and exploited 126 fb^{-1} of $\sqrt{s} = 13$ TeV data. The projection assumes an integrated luminosity of 3000 fb^{-1} for HL-LHC proton-proton collisions at $\sqrt{s} = 14$ TeV. Various systematic uncertainty scenarios are explored. With (without) systematic uncertainties, the discovery significance of the Standard Model Higgs boson pair production is found to be 1.0σ (1.8σ), while the 95% confidence-level upper limit on the HH signal strength is set at 2.0 (1.1). The allowed 68% confidence-interval for the HHH coupling modifier κ_λ is found to be $[-0.5, 6.1]$ ($[0.1, 2.6]$), while the allowed 68% confidence-interval for the $HHVV$ coupling modifier κ_{2V} is $[0.7, 1.4]$ ($[0.7.1.3]$).

Lay Summary

The Higgs boson was found at the Large Hadron Collider (LHC) in 2012, after being predicted nearly 50 years earlier. The Higgs gives mass to other fundamental particles and completes the widely accepted theory of particle physics called the Standard Model (SM). Since its discovery, the way the Higgs is produced has been closely studied and the results match the SM's predictions, but this means there's no evidence of new physics. Producing a pair of Higgs bosons (HH) is much rarer than producing just one and hasn't been seen yet. It's not possible to observe HH production at the LHC, but it might be possible at the upgraded LHC, the HL-LHC. This study aims to investigate the prospect of measuring HH production, when they turn into four b-quarks, using the ATLAS detector at this future HL-LHC.

Preface

The research presented in this thesis is a part of the ATLAS collaboration and would not have been possible without the efforts of the many physicists, engineers, technicians, students, and support staff who make up the ATLAS community. The studies shown here are based on a Run 2 analysis of the $HH \to b\bar{b}b\bar{b}$ final state, which involved a team of approximately 50 members. My main contribution was to extend the analysis to the conditions at the HL-LHC, which involved further examination of the physics and systematic effects and required significant computational resources, including the development of new coding infrastructure capable of processing tens of thousands of simulations for different combinations of parameters, luminosities, and systematic scenarios. I was the main contributor of these extrapolations, but I was guided closely by my group of Maximilian Swiatlowski, Marco Valente and Christopher Gubbels. Figures without references in the caption have been produced by me or in close collaboration with me. Figures with "ATLAS Preliminary" have been approved by the ATLAS collaboration. Figures that I have produced without an ATLAS label or with "ATLAS Internal" have not been approved by the collaboration. The work from this thesis was made public in the form of:

- ATLAS Collaboration. *HL-LHC prospects for the measurement of Higgs boson pair production in the $b\bar{b}b\bar{b}$ final state and combination with the $b\bar{b}\gamma\gamma$ and $b\bar{b}\tau^+\tau^-$ final states at the ATLAS experiment* ATL-PHYS-PUB-2022-053

The primary purpose of this public document is to investigate Higgs pair production in the $b\bar{b}b\bar{b}$ final state at the HL-LHC using the ATLAS detector. I authored most of this section, with significant assistance from Marco Valente during the editing process. The content of the main body of this public document substantially overlaps with the work presented in this thesis. However, this thesis goes beyond the public document by providing additional theoretical and experimental background and analyzing some of the results in greater depth. Moreover, the public document includes a section on the combination of the $b\bar{b}b\bar{b}$ final state with two other final states.

Although I did not write this section, I collaborated with the groups responsible by providing the necessary information and data to obtain the combination results.

Table of Contents

Appendices

List of Tables

List of Figures

Chapter 1

Introduction

Ten years have passed since the discovery of the Higgs boson in 2012 at the Large Hadron Collider (LHC)[1, 2]. In that time, the properties of single Higgs production (H) have been extensively studied. All the measurements regarding the spin and couplings of the Higgs boson are consistent with the predictions of the Standard Model (SM) [3, 4, 5, 6]. As a result, there have been no signs of new physics beyond the SM (BSM) related to the Higgs boson. However, the pair production of the Higgs boson (HH) has yet to be observed and studied due to its significantly lower cross-section, which is 1000 times smaller than that of single Higgs production [7].

The pair production of the Higgs boson through its self-interaction via the coupling λ_{HHH} is of particular interest because within the SM, it relates to the Higgs boson mass m_H and the vacuum expectation value (vev) v via $\lambda_{HHH}^{SM} = \frac{m_H^2}{2v^2}$. The self-coupling λ_{HHH} can be modified by BSM scenarios [8]. Measuring its value would allow for important tests of the mechanism responsible for electroweak symmetry breaking and BSM theories. It would also provide insight into the shape of the Higgs potential, which has far-reaching physical implications. For example, the minimum the universe currently finds itself in within the Higgs potential might not be the true minimum, depending on the shape of the Higgs potential. The universe could therefore transition to the true minimum through quantum tunneling, which could result in a complete alteration of the universe and its physical laws [9, 10]. The Higgs potential's shape also reveals how it changed from its early universe shape to its current shape, and if electroweak baryogenesis occurred, which could explain the matter-antimatter asymmetry [11, 12]. Measuring the final states of HH production allows for the direct constraint of this self-coupling, and thus also BSM theories and the shape of the Higgs potential.

Within the SM, at $m_H = 125$ GeV and $\sqrt{s} = 14$ TeV, HH production is dominant through gluon-gluon fusion (ggF) with a cross-section $\sigma_{ggF}^{SM} = 36.7^{+6\%}_{-23\%}\,(scale{+}m_{top}){+}3.0\%(\alpha_S{+}PDF)$ fb [13, 14, 15, 16]. The uncertainties in the cross-section, known as "scale", "m_{top}", "α_S" and "PDF" are due to the choice of renormalization scheme, the mass of the top quark, the strong coupling constant and the usage of parton distribution functions, respectively. The next leading process for HH production is vector boson fusion (VBF) which within the SM has a predicted cross-section 10 times less than ggF with $\sigma_{VBF}^{SM} = 2.06^{+0.03\%}_{-0.04\%}\ (scale) + 3.0\%(\alpha_S + PDF)\,\text{fb}$ [13].

The search for HH production at the LHC using the ATLAS detector is ongoing. The latest results, from $\sqrt{s} = 13$ TeV proton-proton collisions, have combined HH analyses in the $b\bar{b}b\bar{b}$, $b\bar{b}\tau^+\tau^-$ and $b\bar{b}\gamma\gamma$ decay channels with H analyses in the $\gamma\gamma$, ZZ^*, WW^*, $\tau^+\tau^-$ final states. The integrated luminosity for these results is $126 - 139\,\text{fb}^{-1}$[17]. No significant signal was observed, but an observed (expected) upper limit of 2.4 (2.9) was set on the HH signal strength, $\mu = \sigma_{ggF+VBF}/\sigma_{ggF+VBF}^{SM}$, at a 95% confidence level (CL). The signal strength μ is calculated as the sum of the ggF HH and VBF HH cross-sections, divided by the same cross-section in the SM scenario.

A major upgrade to the LHC, the High Luminosity LHC (HL-LHC), is set to be complete around 2027. The upgraded accelerator is then expected to deliver a total integrated luminosity between 3000 fb^{-1} and 4000 fb^{-1} with $\sqrt{s} = 14$ TeV until around 2040. The increase in center of mass energy and substantial increase in luminosity make the HL-LHC an ideal location to study HH production. A recent projection to the HL-LHC with an integrated luminosity of 3000 fb^{-1} and $\sqrt{s} = 14$ TeV found a signal significance of 4.0σ with systematic uncertainties and 4.5σ without systematic uncertainties [18]. This study used a combination of ATLAS and CMS analyses conducted in the $b\bar{b}b\bar{b}$, $b\bar{b}\tau^+\tau^-$, $b\bar{b}\gamma\gamma$, $b\bar{b}VV$ and $b\bar{b}ZZ$ final states using early Run 2 LHC data. These recent studies show not only strong constraints on HH production at the HL-LHC are possible, but also potentially discovery and measurements of this process's properties.

This thesis presents the latest extrapolations for the $HH \to b\bar{b}b\bar{b}$ process. These extrapolations are based on the $HH \to b\bar{b}b\bar{b}$ analysis performed on the available Run 2 data of 126 fb^{-1} using the ATLAS detector [19]. This Run 2 result yielded an observed (expected) signal strength upper limit of 5.4 (8.1) at a 95% CL. The observed (expected) constraints on the signal strength μ were found to be [-3.9, 11.1] ([-4.6, 10.8]) at a 95% CL. These results, which include a new data-driven background estimate, categorization strategies and jet pairing techniques, improve on the previous $HH \to b\bar{b}b\bar{b}$ projections based on 27.5 fb^{-1} [20, 21, 22]. The goal of this note is to use these improvements to explore the sensitivity of the $HH \to b\bar{b}b\bar{b}$ analysis at the HL-LHC.

Chapter 2

Introduction to Theoretical Background

This section seeks to offer the theoretical background to aid in comprehending the principal workings and outcomes of this thesis. The explanations provided take inspiration from references [23] and [24].

The Standard Model (SM) is a theory that describes the most fundamental known particles in the universe, as well as the interactions between them. It is based on the framework of quantum field theory (QFT). Within QFT, the terms “particles” and “fields” are commonly used interchangeably; however, it is important to clarify that the fields are the fundamental aspect of the theory, not the particles. These fields are responsible for producing particles, which are tiny localized fluctuations within the fields. For example, there is only one electron field for the entire universe. All electrons (and positrons) in the universe are small fluctuations in this one quantum field, and the same is true for the other fundamental fields and particles. Figure 2.1 summarizes all the fundamental fields within the SM, detailing their masses, spins, electric and color charges [25]. The fundamental fields that correspond to matter are the 12 fermions: six quarks and six leptons. Both the six quarks and leptons can be organized further into three generations. The first generation consists of the up quark, down quark, electron, and electron neutrino. The other two generations can be thought of as replicas of the first generation, with the same structure but with each corresponding particle being heavier for each consequent generation.[1]

2.1 Gauge theory and groups

The framework of QFT can describe freely propagating particles, but this is not enough for particle physics since it is known that these particles have interactions. To go from a theory with just QFT and freely propagating particles to a theory with interactions such as quantum electrodynamics

[1] With the exception of the three neutrinos masses which haven’t been measured yet.

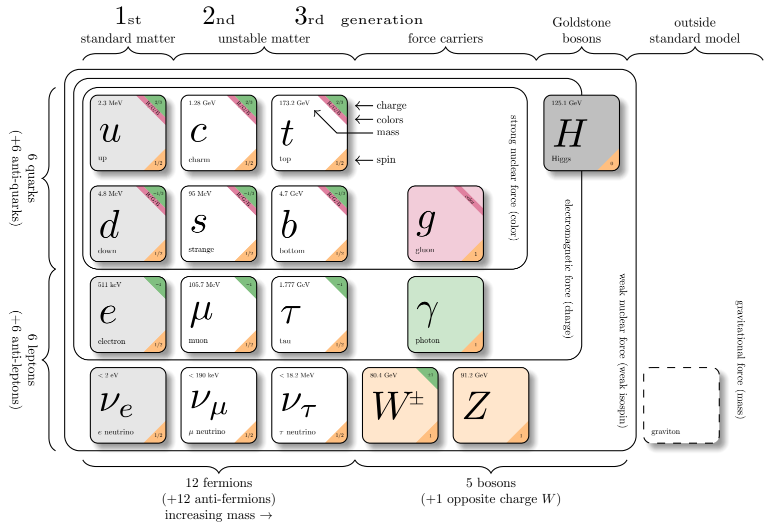

Figure 2.1: Pictorial summary of all the particles within the SM as well as detailing their masses, spins, charges and color. The diagram does not include the anti-particles, where there is one for each fermion shown with the same mass and spin but opposite electric and color charge. [25]

(QED) or quantum chromodynamics (QCD), one needs to take an additional step. This step is the implementation of gauge symmetries into the theory [26]. A theory is said to exhibit a gauge symmetry when the resulting physics remains unchanged under local transformations. These transformations can be mathematically described using group theory. In this context, the group's elements are the transformations and the representations of the group are the fields or particles that the transformations act on. Groups used in particle physics are Lie groups. A Lie group governs the class of transformations where an infinitesimal transformation can be used to construct any arbitrary transformation. For example, a 60 degree rotation can be constructed from many small 1 degree rotations. Transformations can be written as matrices; for example, counterclockwise rotations R around the origin in the xy plane through an angle θ can be written as:

$$R_{xy}(\theta) = \begin{bmatrix} cos\theta & -sin\theta \\ sin\theta & cos\theta \end{bmatrix} \tag{2.1}$$

A property of Lie groups is that the transformations can be expressed using an exponential map, as follows:

$$A = e^{ig_A \cdot v^A} \tag{2.2}$$

where g_A are referred as the generators of the group, providing the basis to generate the transformation A, while v^A parameterizes the transformation. To explain this further, consider rotations in three dimensions, which are elements of a group called $SO(3)$. In the case of $SO(3)$, one needs a generator for each plane of rotation, three in total: rotations along the xy, xz and yz planes. Any transformation within the group can be performed through a linear combination of the generators. The proportion of each generator utilized is determined by the parameters v^A:

$$g_A \cdot v^A = g_{xy}\alpha + g_{xz}\beta + g_{yz}\gamma \tag{2.3}$$

where α, β, and γ are the specific parameters for the generators g_{xy}, g_{xz}, and g_{yz}, respectively. An explicit matrix form for the $SO(3)$ generators are[2]:

$$g_{xy} = \begin{pmatrix} 0 & i & 0 \\ -i & 0 & 0 \\ 0 & 0 & 0 \end{pmatrix} \qquad g_{xz} = \begin{pmatrix} 0 & 0 & -i \\ 0 & 0 & 0 \\ i & 0 & 0 \end{pmatrix} \qquad g_{yz} = \begin{pmatrix} 0 & 0 & 0 \\ 0 & 0 & i \\ 0 & -i & 0 \end{pmatrix} \tag{2.4}$$

Performing the Taylor expansion for the g_{xy} generator alone (using θ as the parameter instead of α) yields:

$$R_{xy}(\theta) = e^{ig_{xy} \cdot \theta} = I + ig_{xy}\theta + \frac{1}{2!}(ig_{xy}\theta)^2 + \frac{1}{3!}(ig_{xy}\theta)^3 + ... \tag{2.5}$$

Then, by substituting the matrix form for the generator g_{xy}, which can be found in equation 2.4, one obtains:

$$R_{xy}(\theta) = \begin{pmatrix} 1 - \frac{1}{2!}\theta^2 + ... & -\theta + \frac{1}{3!} + \theta^3... & 0 \\ \theta - \frac{1}{3!}\theta^3 + ... & 1 - \frac{1}{2!}\theta^2 + ... & 0 \\ 0 & 0 & 1 \end{pmatrix} = \begin{pmatrix} cos\theta & -sin\theta & 0 \\ sin\theta & cos\theta & 0 \\ 0 & 0 & 1 \end{pmatrix} \tag{2.6}$$

yielding the same result as given in equation 2.1, but in three dimensions.

2.2 Symmetries and the Form of the Lagrangian

Interactions are introduced into the theory by ensuring that the laws of physics remain unchanged under local transformations. These transforma-

[2]These set of three generators for $SO(3)$ are not unique, theres many different sets.

tions were introduced in the previous section, but it may not be immediately clear how they can be applied to the laws of physics. This is where Lagrangians come into play. In particle physics, the laws of physics are generally described by a Lagrangian $\mathcal{L}$. Lagrangians provide an effective method for implementing and enforcing these local symmetries. For example, consider a theory with a complex scalar field ϕ without interactions, described by the following Lagrangian[3]:

$$\mathcal{L} = \partial_\mu \phi \partial^\mu \bar{\phi} + m^2 \phi \bar{\phi} \tag{2.7}$$

Rotations in three dimensions belonging to the $SO(3)$ group were looked at previously in section 2.1.[4]. Now, consider a simpler group called $U(1)$. It is composed of unitary matrices of dimension one, which are simply complex numbers with a norm of one. They can also be expressed as an exponential map in the form of $e^{i\theta}$, where $\theta \in [0, 2\pi)$. If one applies one of these transformations, $e^{i\theta}$, to the Lagrangian, where θ is constant for all positions in space-time X^μ but arbitrary otherwise, then the fields will transform as follows:

$$\phi \rightarrow \phi' = e^{i\theta}\phi \qquad\qquad \bar{\phi} \rightarrow \bar{\phi}' = e^{-i\theta}\bar{\phi} \tag{2.8}$$

The entire Lagrangian will transform like the following:

$$\mathcal{L} \rightarrow \mathcal{L}' = \partial_\mu \phi' \partial^\mu \bar{\phi}' + m^2 \phi' \bar{\phi}' \tag{2.9}$$

Using the forms shown in eq 2.8 to substitute in ϕ' and $\bar{\phi}'$ gives:

$$\mathcal{L}' = (\partial_\mu e^{i\theta}\phi)(\partial^\mu e^{-i\theta}\bar{\phi}) + m^2 (e^{i\theta}\phi)(e^{-i\theta}\bar{\phi}) \tag{2.10}$$

Because $e^{i\theta}$ and $e^{-i\theta}$ are constants, they can be moved through the derivatives ∂ and fields ϕ, which results in:

$$\mathcal{L}' = (e^{i\theta}e^{-i\theta})\partial_\mu \phi \partial^\mu \bar{\phi} + (e^{i\theta}e^{-i\theta}) m^2 \phi \bar{\phi} = \mathcal{L} \tag{2.11}$$

This is an example of the Lagrangian (and the laws of physics) remaining unchanged under *global* $U(1)$ transformations. However, as mentioned previously, gauge theory requires the Lagrangian to remain unchanged after applying *local* transformations. Local transformations require the value of

[3]This is the Lagrangian formulation of the Klein-Gordan equation.

[4]Where the S in SO(3) stands for "Special" meaning that the matricies representing transformations in the group have a determinant of 1, and the O means they have to be orthogonal

θ to depend on one's local position in space-time X^μ, resulting in the fields transforming as follows:

$$\phi \rightarrow \phi' = e^{i\theta(X^\mu)}\phi \qquad\qquad \bar{\phi} \rightarrow \bar{\phi}' = e^{-i\theta(X^\mu)}\bar{\phi} \tag{2.12}$$

As previously shown in eq 2.11, $e^{i\theta}$ and $e^{-i\theta}$ are constants and can be moved through the derivatives, eventually canceling each other out. Now, $e^{i\theta(X^\mu)}$ and $e^{-i\theta(X^\mu)}$ are not constants due to their dependence on X^μ, resulting in:

$$\mathcal{L}' = (\partial_\mu e^{i\theta(X^\mu)}\phi)(\partial^\mu e^{-i\theta(X^\mu)}\bar{\phi}) + (e^{i\theta(X^\mu)}e^{-i\theta(X^\mu)})m^2\phi\bar{\phi} \neq \mathcal{L} \tag{2.13}$$

This Lagrangian is no longer invariant under local transformations. The Dirac Lagrangian describes the behavior of freely propagating spin-$\frac{1}{2}$ matter particles, fermions, such as leptons and quarks. However, similar to eq 2.13, which describes spinless particles, the Dirac Lagrangian is not initially invariant under local $U(1)$ transformations. Although not shown in full mathematical rigor, the next section will explain the process of going from the Dirac Lagrangian to the SM. This process involves enforcing the invariance of the Lagrangian under local transformations, which will introduce interactions through the electromagnetic, weak, and strong forces that are not originally present in the Dirac Lagrangian.

2.3 The Standard Model

The Dirac Lagrangian describes freely propagating fermions like leptons and quarks, but it is not initially symmetric under local $U(1)$ transformations. To enforce symmetry, an additional field, A_μ, is introduced. This field is chosen to transform in a way that keeps the Lagrangian invariant. These additional fields, A_μ, are called gauge fields. One is needed for each generator of the group. In the case of $U(1)$, only one gauge field is needed, which corresponds to the photon of the electromagnetic force in quantum electrodynamics (QED).

The strong force, or quantum chromodynamics (QCD), is similar to QED, but with some key differences. One can get QCD by enforcing symmetry[5] under $SU(3)$ transformations. $SU(3)$ is a group of 3×3 matrices that are unitary like $U(1)$, but with the extra constraint that they must have a determinant of one[6]. $SU(3)$ has eight generators, which means it has eight gauge bosons, the gluons.

[5] symmetry and invariance are used interchangeably

[6] Which is what the “S” stands for in SU

Unlike QED, which is a symmetry for all particles carrying electric charge, QCD is only a symmetry for quarks that carry color charge. In QED, there is only one type of charge, and the photon transforms particles between different states of this electric charge. In total, there are two possible states of electric charge: positive and negative. In QCD, there are three types of color charge: red, blue, and green. The gluons transform quarks between different states of color, which include six in total: red, anti-red, blue, anti-blue, green, and anti-green.

Another difference is that, unlike QED, which has an abelian symmetry, QCD has a non-abelian symmetry. This means that the matrices in the group don't commute, and the order of transformations matters. The physical consequence of this non-abelian symmetry is that the gluons interact with each other, while photons don't. This non-abelian aspect of QCD explains the short range of the strong force, along with hadronization and color confinement.

The weak force is different from the strong and electromagnetic force because it reflects a broken symmetry. This broken symmetry is related to the fact that the gauge bosons for the weak force (the Z and W bosons) have mass. One cannot form a locally symmetric gauge theory with just the weak interaction, but one can if it's combined with electromagnetism to form electroweak theory.

Although the electroweak theory is symmetric in principle, it's not a current symmetry of the SM. However, it was a symmetry during the early universe when the universe was very hot. As the universe cooled, it underwent a phase transition, resulting in the broken symmetry observed today, along with the massive Z and W bosons. Another important aspect to consider is that adding masses to fermions breaks the gauge symmetries that have been previously introduced. It is not possible to simply add masses to the gauge theories of $U(1)$ and $SU(3)$. However, masses can be generated through another means, the Higgs mechanism. This mechanism breaks electroweak symmetry and provides masses to the fermions and weak gauge bosons, thereby completing our understanding of the Standard Model.

While the SM is able to explain many aspects of particle interactions, the SM is not a complete theory of the universe. Some of the main issues with the SM are that it is unable to explain the force of gravity, dark matter and neutrino masses [27, 28, 29]. Another failure of the SM is that it cannot explain the matter-antimatter asymmetry of the universe [11]. The following section explores one possible solution that can be provided through the Higgs mechanism, and motivates the search for Higgs pair production, a main topic in this thesis.

Chapter 3

The Higgs Mechanism

It was previously mentioned that fields are fundamental, and that particles are just fluctuations on top of the fields. To describe the field ϕ, one can think of expressing the tiny fluctuations $\delta\phi$ (which represent observable particles) on top of the pre-existing non-fluctuating field ϕ_0, which can be thought of as a background. The field can be expressed as $\phi = \phi_0 + \delta\phi$.

Given a theory that includes the field ϕ, one can find solutions for ϕ_0 that satisfy the laws of physics encoded by the Lagrangian. Then, by considering the fluctuations around the ϕ_0 solution, we can understand the behavior of the observable particles $\delta\phi$ associated with ϕ. When $\phi_0 = 0$ is a solution, the resulting fluctuations around it corresponding to the observable particles are all massless and have a localized symmetry. However, if $\phi_0 \neq 0$, a background field that is not trivially zero everywhere, the resulting physics produces particles with mass and breaks the localized symmetry [23, 24].

This is what happens with the Higgs field in the SM, which causes electroweak symmetry breaking (EWSB) and gives the weak bosons mass in the process. The Higgs field, denoted by ϕ, has four components or degrees of freedom. These four components (h_1, h_2, h_3, h_4) are arranged into a complex doublet under $SU(2)$ transformations.

$$\phi = \begin{pmatrix} h_1 + ih_2 \\ h_3 + ih_4 \end{pmatrix} \tag{3.1}$$

It is important to distinguish between the Higgs field, denoted by ϕ, and the Higgs boson, denoted by h. They are deeply connected, but they are not the same thing. The Higgs field is the fundamental field. The Higgs boson is a small fluctuation in the Higgs field, one of its four degrees of freedom. It only emerges after EWSB. It manifests itself as a physically observable scalar particle, being observed at the LHC in 2012 with a mass of 125 GeV.

Before EWSB, all four degrees of freedom of the Higgs field were massless scalar particles, and there was no Higgs boson. Only after EWSB did one of these degrees of freedom become the Higgs boson, while the other three degrees of freedom were absorbed by the three weak gauge bosons, giving them mass.

The form of the Higgs potential allows the Higgs field to obtain a non-zero background value ($\phi_0 \neq 0$), also referred to as the vacuum expectation value (vev). The potential is encoded in the Standard Model (SM) Lagrangian in the following form:

$$V(\phi) = -\mu^2 \phi^\dagger \phi + \frac{1}{4}\lambda^2 (\phi^\dagger \phi)^2 \tag{3.2}$$

In order to fully visualize the Higgs potential, one would need five dimensions: one dimension for the value of the potential $V(\phi)$, and four dimensions for each component of the Higgs field (h_1, h_2, h_3, h_4). However, it is not possible to visualize all four of the Higgs components at once. It is useful to show a simplified version of the potential in terms of just one or two of the Higgs field's components. Despite this simplification, the characteristics of EWSB and the Higgs mechanism can still be captured. Therefore, diagrams shown here will only use one of the four Higgs field components, labeled as the "Higgs field parameter", while the other three components are assumed to be equal to zero. The background value for the Higgs field and the resulting fluctuations representing particles must be solutions (minima or maxima) of the Higgs potential. The Higgs field occupying a given solution is often represented as a particle itself, which is sometimes referred to simply as the "Higgs". An example of this can be seen in figure 3.1a.

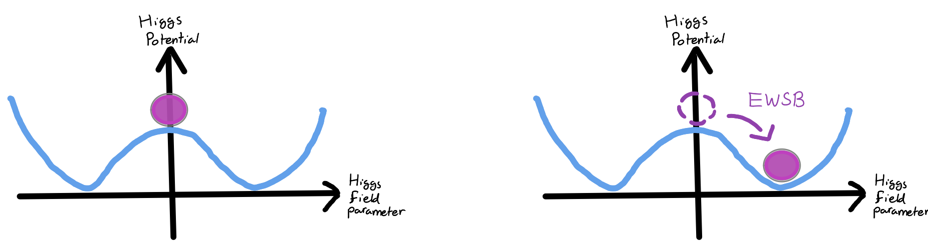

(a) Before EWSB

(b) After EWSB

Figure 3.1: Visual illustration of electroweak symmetry breaking (EWSB) through the Higgs mechanism.

The Higgs potential, shown in figure 3.1a, has a shape known as a "Mexican hat". This shape has the right properties to allow for EWSB. Before EWSB, the Higgs occupied the solution at the maximum of the potential in the middle. At this maximum point, the potential and the background value of the Higgs field is zero, and the fluctuations around it result in physics that exhibit a localized symmetry. This symmetry can be seen visually by imagining the Higgs sitting on top of the potential and reflecting the potential around the y-axis. After this reflection, the resulting shape of the potential will be the same, indicating that there is a symmetry present.

The solution at the maximum is unstable. Eventually, the Higgs will roll down from the maximum to one of the available minima, either to the left or the right. As an example, figure 3.1b shows the Higgs rolling to the right. When the Higgs rolls down the potential, the background value of the Higgs potential is no longer zero, breaking the symmetry.

Similar to how the symmetry was visible when the Higgs was at the maximum of the potential, the broken symmetry can also be visible. For example, assume the Higgs decays to the right minimum, as shown in figure 3.1b. If the potential is reflected around the y-axis, it will no longer look the same. This is because the Higgs will be reflected from the right minimum to the left minimum, indicating a broken symmetry.

This non-zero value and broken symmetry give mass to the weak gauge bosons and fermions, with the mass being proportional to the acquired vev. The direction in which the Higgs falls, either to the left or the right, is random and arbitrary, which is why the process is called a *spontaneous* symmetry breaking.

3.1 Higgs pair production and shape of Higgs potential

The shape of the Higgs potential after EWSB can be rewritten in a more telling way by expanding around the minimum in terms of the physically observable Higgs boson h. It can be written as:

$$V(h) = V_0 + \lambda v^2 h^2 + \kappa_\lambda \lambda v h^3 + ... \tag{3.3}$$

where V_0 is an arbitrary constant representing the non-zero height of the potential, v is the vev and κ_λ is the coupling modifier.

The precise shape of the Higgs potential is not known. The part that has been measured is based on the Higgs physical mass, which corresponds to the $\lambda v^2 h^2$ term in Equation 3.3. However, the full picture of the Higgs potential is not shown in Equation 3.3. Contributions from higher-order terms in the Lagrangian, related to the Higgs interacting with other particles, can alter the stability and shape of the potential. This is explored further in Section 3.2. The next term from Equation 3.3 that can be measured is the cubic term, h^3, also known as the tri-linear coupling. This term represents

Higgs self-interaction and enables Higgs pair production. The Higgs self-interaction is parameterized by κ_λ and in the SM scenario, $\kappa_\lambda = 1$. The Feynman diagrams for Higgs pair production are shown in figures 3.2 and 3.3. From these diagrams, it can be seen that the κ_λ term appears in some of the diagrams, figure 3.3b and figure 3.2a. The other diagrams also introduce further couplings, such as the Higgs to the top quark (parameterized by κ_t), the VVH[7] coupling (κ_V), and the VVHH coupling (κ_{2V}). Within the SM, the parameters relating to these couplings ($\kappa_t, \kappa_V, \kappa_{2V}$) are also equal to one. The work done in this thesis is not able to probe the other couplings apart from κ_{2V}. The parameter κ_{2V} offers an insight into the gauge structure of the Higgs and the results of this work can be found in section 7.3.

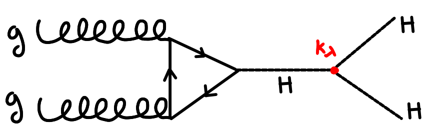

(a) ggF tri-linear coupling

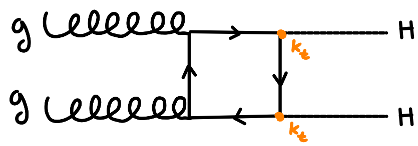

(b) ggF box diagram

Figure 3.2: ggF HH production Feynman diagrams

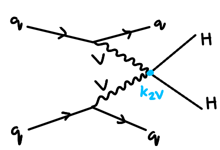

(a) VBF VVHH vertex

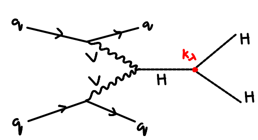

(b) VBF tri-linear coupling

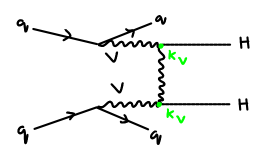

(c) VBF κ_V^2 production mode

Figure 3.3: VBF HH production Feynman diagrams

Studying HH production can provide insight into the Higgs self-coupling and the shape of the Higgs potential. This Higgs self-coupling has yet to be measured precisely, making it an important area of study. Moreover, the shape of the Higgs potential holds clues to both the death and birth of the universe, which makes it an even more fascinating subject of study, as will be explored in the next two sections [9, 11].

[7] Where "V" represents a vector boson, so either a W or Z boson

3.2 Instability of Higgs potential and death of universe

As previously stated, the current understanding of the shape of the Higgs potential is primarily based on the Higgs physical mass, M_h , represented by the h^2 term in Equation 3.3. However, external contributions from higher-order terms in the Lagrangian that describe the interaction between the Higgs and other particles can also impact the shape of the potential. As the Higgs interacts more with heavier particles, this effect is largely dominated by the mass of the top quark, M_t, which is currently the heaviest known fundamental particle[8]. Current best measurements [7] of the Higgs mass M_h and the top mass M_t are:

$$M_h = 125.25(17)\text{ GeV}, \qquad M_t = 173.2(9)\text{ GeV} \tag{3.4}$$

The relationship between the stability of the universe and the Higgs potential can be seen in figure 3.5. The figure illustrates three different scenarios: a stable potential in green, a meta-stable potential in orange, and an unstable potential in red. If the Higgs potential is either meta-stable or unstable, it means that the minimum that the Higgs currently finds itself in is not a true minimum. In this scenario, the Higgs could potentially quantum tunnel down the potential. This would happen through a barrier[9]. Once the Higgs goes down the potential, it acquires a different non-zero vev, changing the mass of all the fundamental particles. This would result in a change in the laws of chemistry, and the fine-tuning of both large and small scale structures, effectively bringing an end to the current universe.[10] According to the plot in figure 3.4, the current experimental values of M_t and M_h suggest that the Higgs potential and the universe are metastable, on the edge of stability. Investigating HH production further could provide more information about the exact stability of the universe.

[8]BSM physics could also play a role here in the stability of the Higgs potential. For example, a possible explanation for neutrino masses is the type I see-saw mechanism, which predicts a heavy right-handed neutrino. Like the top quark, its large mass would greatly affect the shape of the Higgs potential.

[9]A barrier is a peak in the potential separating the two minima

[10]This change in the Higgs would happen somewhere in locally in the universe, inside a bubble, that would soon expand, very quickly reaching the speed of light and destroying everything in the way. [9]

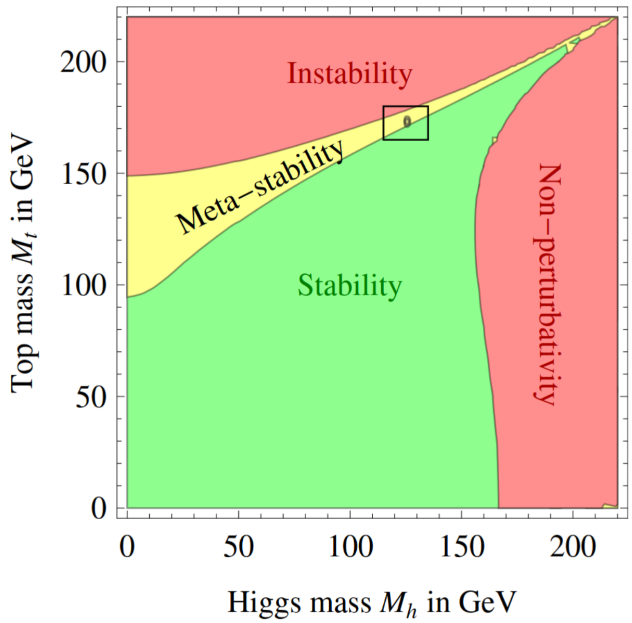

Figure 3.4: Showing the stability of the SM Higgs potential in term of the mass of top quark M_t against mass of Higgs M_h via[9]

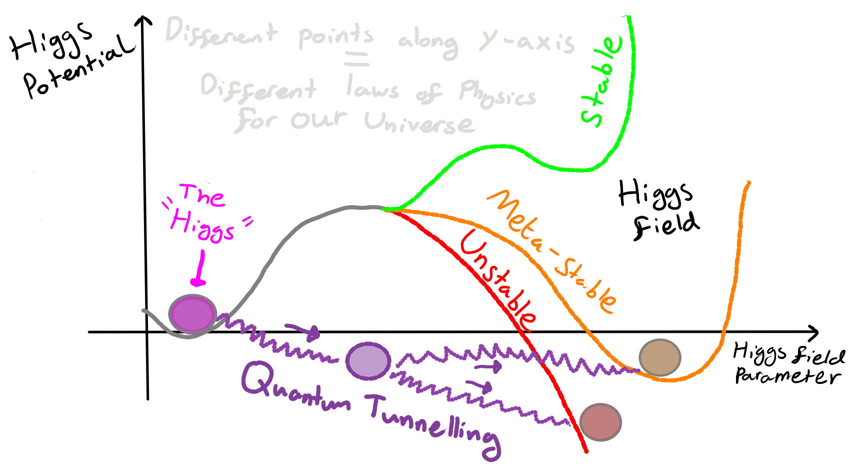

Figure 3.5: Instability of the Higgs potential

3.3 Electroweak baryogenesis and birth of universe

Conventional QFT as introduced previously is suitable for making predictions in empty space-time. This works well for making predictions on observables such as cross-sections at particle colliders. However, the extremely high temperatures of the early universe also had a significant matter and radiation density, making the conventional QFT approach inadequate. Combining elements of thermodynamics to take into account the conditions of the early universe suggests that the shape of the Higgs potential depends on temperature.

Since the temperature has changed dramatically since the early universe, the shape of the Higgs potential has also changed. This change in the shape of the Higgs potential explains how the Higgs field came to be at the maxima of the potential, despite the fact that the solution at the maximum is unstable. In the early stages of the universe, the solution at $\phi_0 = 0$ was stable, as depicted in figure 3.6a. However, as the universe cooled, this solution became unstable, as shown in figure 3.6b. Eventually, the Higgs decayed into one of the minima solutions, leading to EWSB, as illustrated in figure 3.6c. The early universe Higgs potential also has interesting consequences

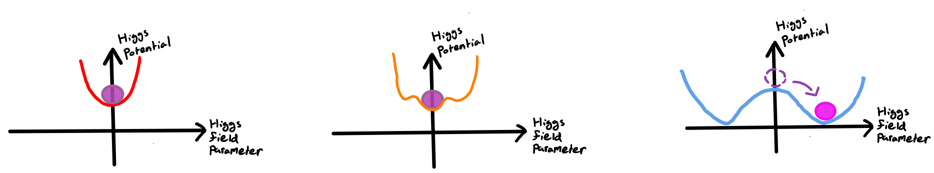

(a) Early universe (b) Intermediate stage (c) Today

Figure 3.6: Illustrative example of how Higgs potential transitioned from early universe to some exemplary intermediate stage to the shape today explaining how it could end up with a unstable maxima solution.

for some of the shortcomings of the SM. One of these shortcomings is the lack of antimatter currently observed in the universe. Electroweak baryogenesis is one proposed mechanism that provides an explanation to solve this matter-antimatter asymmetry problem [11]. In order for electroweak baryogenesis to occur, the three Sakharov conditions [30] must be met. These conditions are:

1. Baryon number violation

2. C and CP violation

3. Out of equilibrium interactions

In the SM, baryon violation can occur through the process of sphalerons[31], which are non-perturbative phenomena that cannot be described by traditional Feynman diagrams. Sphalerons convert three baryons into three anti-leptons, or three anti-baryons into three leptons, and vice versa. However, due to high suppression from the Higgs vev, sphalerons do not appear to have a measurable rate post-EWSB [32]. Since sphalerons also allow for the production of anti-baryons, there must be C and CP violation to ensure that the process of producing baryons is greater than the process of producing anti-baryons. This can be also already be achieved within the Standard Model through the complex phase of the CKM matrix [33]. The CP violation within the SM may not be sufficient, but there are several BSM theories that include the necessary additional amount [34].

In the SM, the transition of the shape of the Higgs potential from the early universe to today could occur smoothly, as demonstrated by the brown arrows in figure 3.7. However, this smooth transition would not satisfy Sakharov's third condition of out-of-equilibrium dynamics. The out of equilibrium dynamics is possible when the Higgs potential undergoes a strong first order phase transition as shown by the green arrows in figure 3.7. This phase transition occurs when the shape of the intermediate Higgs potential has barriers, similar to the death of the universe. With these barriers, localized pockets of the Higgs field can quantum tunnel through the barriers and into the minima with non-zero vev's. The out of equilibrium dynamics comes from the fact that matter and antimatter have different probabilities to quantum tunnel through the barrier, thus satisfying the final condition for electroweak baryogenesis. Although model-dependent, some models suggest that a value of κ_λ greater than 1.5 is required for a strong first-order phase transition and electroweak baryogenesis to occur [35]. Hence, a precise measurement of this parameter could provide insight into something fundamental about the early history of the universe.

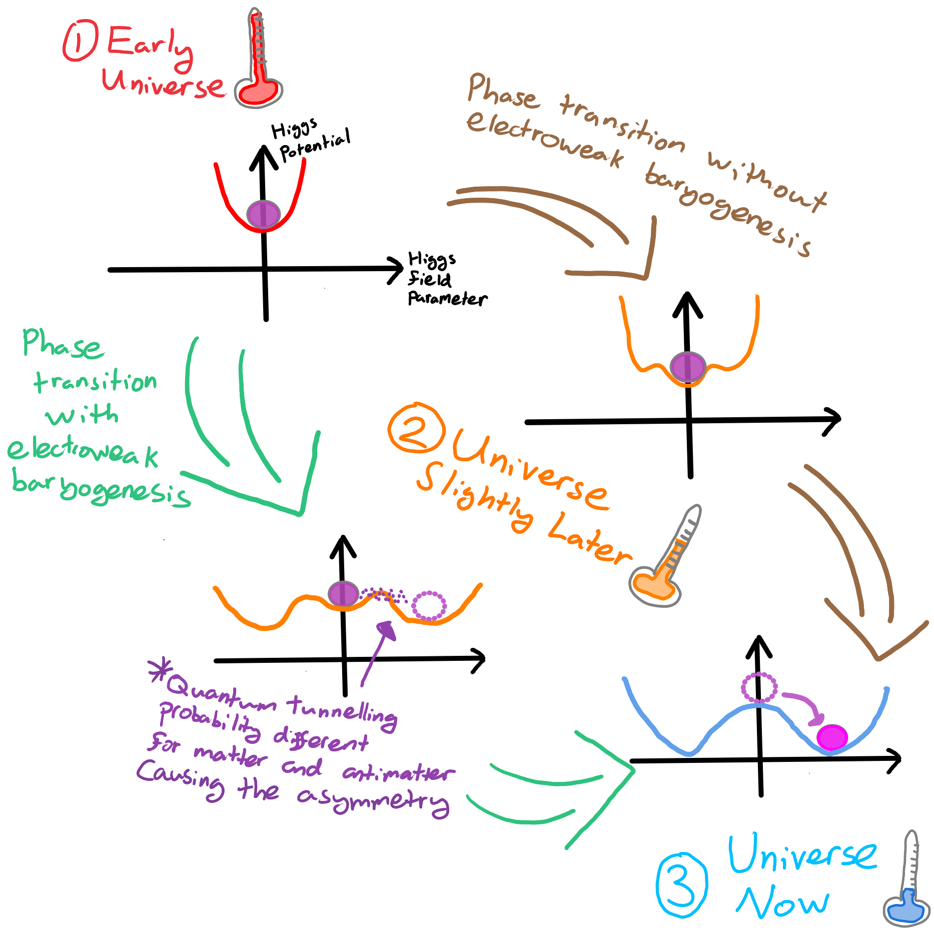

Figure 3.7: Possible electroweak baryogenesis via a first order phase transition of Higgs potential

Chapter 4

ATLAS detector

4.1 The Large Hadron Collider

The Large Hadron Collider (LHC) is a 27 km long particle accelerator located 100 m underground at CERN near Geneva, Switzerland. Within the LHC, two beams of protons are accelerated close to the speed of light. The beams travel in opposite directions and are brought together to collide the particles. The beams are guided around the circular accelerator by superconducting dipole magnets that must be cooled to $-271.3\,^{\circ}\mathrm{C}$ (1.9 K). The beams of particles also have to be kept in an ultra-high vacuum in order to prevent collisions between the accelerating particles and contaminating gas particles.

The points where the beams collide are called interaction points, and detectors and experiments are built around each of these four points to measure the resulting physics from the collisions. These detectors include ATLAS, CMS, LHCb, and ALICE, with the latter being unique in that it is primarily designed for studying the collisions of heavy ions. The LHC's Run 2, which is used in the projections of this thesis, provided proton-proton collisions at a center-of-mass energy of 13 TeV. Before the LHC can accelerate the protons to this energy, it uses a series of smaller accelerators and machines to gradually build up the energy and speed of the particles. The whole chain of accelerators, including the LHC, is outlined in figure 4.1.

4.2 ATLAS at LHC

The ATLAS detector is a multi-purpose detector that is built to maximize its physics program and discovery potential within the bounds of the LHC. Figure 4.2 shows a full schematic of ATLAS with all of its major sub-detectors and subsystems labeled. The inner detector (ID) is the innermost part of the detector[38], sitting only 3.3 cm away from the interaction point where the protons collide. The ID is composed of three sub-systems: the silicon pixel

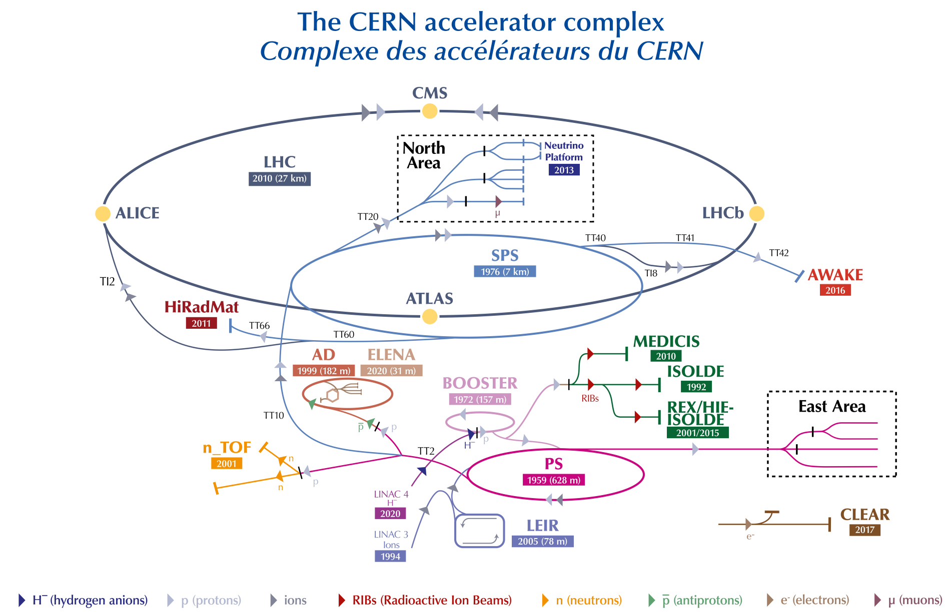

[redacted]

Figure 4.1: CERN accelerator's complex including the LHC[36][37]

detector, the semiconductor tracker, and the transition radiation tracker. With a total radius of 1.2 m and length of 6.2 m along the beam pipe, the ID provides coverage of $|\eta| < 2.5$. The ID is embedded within a 2 Tesla homogeneous magnetic field, causing the tracks of charged particles to curve, enabling the determination of the particle's momentum. Surrounding the ID and just outside the solenoid magnetic is the electromagnetic and hadronic calorimeters. These measure the energy of both neutral and charged particles, absorbing the energy as the particles travel through them, with a total coverage of $|\eta| < 4.9$[39].

The outermost part of the detector is the muon spectrometer (MS). The MS is a large tracking system that is mainly used to detect, track and measure the momentum of muons that easily escape from the inner parts of the detector [40]. The MS provides a total coverage of $|\eta| < 2.7$. The MS is similar to the ID in that they both use magnetic fields to curve charged particles so that their momentum can be measured. However, the

MS is much larger, with less spatial resolution, and uses a toroidal magnetic configuration.

ATLAS has a two-layered trigger system to select events for recording [41]. The first layer is the hardware-based Level-1 (L1) trigger, which is used to make coarse elementary cuts and dramatically reduce the data rate from 40 MHz to 100 kHz. The L1 trigger is then followed by the software-based High-Level Trigger (HLT), which uses more sophisticated algorithms to pick events of most interest and further reduce the data rate to a manageable final 1 kHz.

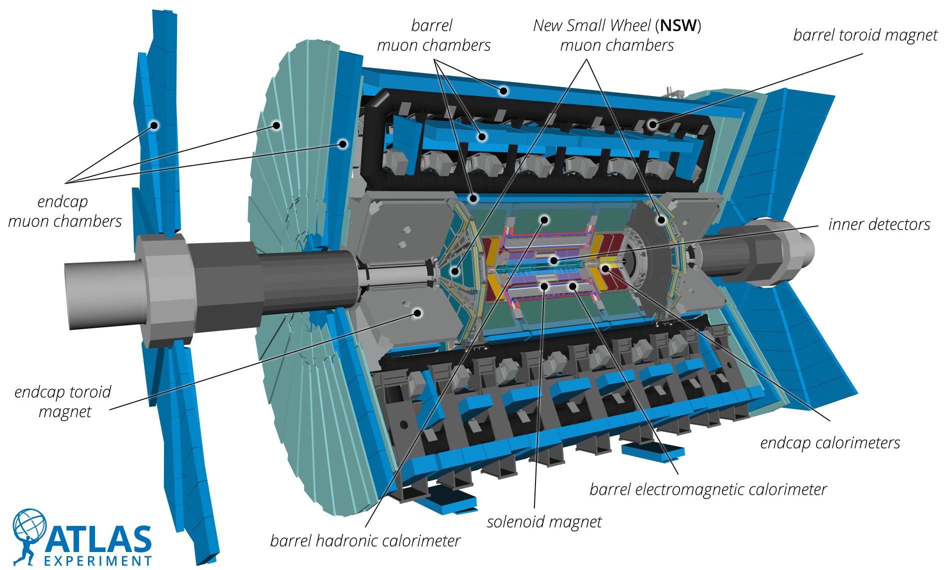

Figure 4.2: Full schematic of ATLAS: A large Toroidal LHC Apparatus[37]

4.3 ATLAS at HL-LHC

The High Luminosity Large Hadron Collider (HL-LHC) will collide protons at an increased instantaneous luminosity by a factor of five to seven compared to the LHC era. With this increased instantaneous luminosity comes an increase in pile-up, which is the number of proton-proton collisions that occur along the beam-pipe within the detector during each proton bunch crossing. The pile-up during 2016 was around 25, while the pile-up expected at the HL-LHC is 140-200. The nominal integrated luminosity will also increase by more than a factor of ten, resulting in a substantial increase in radiation damage to many of the detector components, electronics, and other detector materials such as glue and cabling.

ATLAS has various planned upgrades to its sub-detectors and trigger to help it cope with the radiation damage and pile-up expected from the conditions at the HL-LHC[42]. All three sub-systems of the ID will be replaced by a completely silicon system called the Inner Tracking Detector (ITK). The ITK will extend the tracking coverage to $|\eta| < 4$ while providing a reduced material budget, higher granularity, and a higher read-out bandwidth. The improvement from the ITK will mean many key reconstruction techniques such as b-tagging will be able to maintain their performance even in an environment with a substantial increase in pile-up. Since b-tagging is crucial in the studies of $HH \to b\bar{b}b\bar{b}$, a dedicated section exploring the results of different future b-tagging performances in section 7.6 is included.

The majority of pile-up interactions will be soft, which means that there will be an increase in particles and occupancy in the forward directions of the detector. In this area, the granularity of the calorimeters is coarser and the momentum resolution of the ITK is worse. To address this, the high-granularity timing detector (HGTD) will be installed in the forward regions, in front of the end-cap calorimeters. The HGTD will provide more timing information of charged particles, which will aid in the rejection of tracks coming from pile-up interactions. Additionally, the muon spectrometer (MS) will be upgraded to improve the trigger, including removing gaps to improve trigger efficiency and reducing the fake trigger rate in the forward regions. Improvements will also be made to the trigger and data acquisition systems to increase the bandwidth readout and maintain a high signal acceptance, despite the increased occupancy and pile-up from the HL-LHC's higher data rate.

The current baseline trigger and data acquisition system includes a hardware level-0 (L0) trigger. This trigger has a maximum output rate of 1 MHz and 10 μs latency, using muon and calorimeter information. The system also includes a software-based event filtering. This uses tracking information and more sophisticated algorithms than L0 to provide a final output rate of 10 kHz [43]. With the HL-LHC output rate of 10 kHz, compared to the Run 2 rate of 1 kHz, ten times more data can be stored. The increased bandwidth and improved information at the trigger level will help maintain trigger thresholds even with more jets from higher pile-up events. As a result, more data and events are outputted from the trigger, and the process of identifying events with interesting physics can be performed offline using more advanced algorithms.

Chapter 5

Run 2 Analysis

5.1 Data

These projections are based on the $HH \to b\bar{b}b\bar{b}$ analysis that was performed on LHC proton-proton (pp) collision data at a center-of-mass energy of $\sqrt{s} = 13$ TeV, which was collected during the LHC Run 2 [19]. Since the SM branching ratio of $H \to b\bar{b}$ is 58.2%, around one third of all HH events decay into $b\bar{b}b\bar{b}$, making it the most common di-Higgs final state [7]. This makes $HH \to b\bar{b}b\bar{b}$ an important channel for studying HH.

For this analysis, data was collected in the years 2016, 2017, and 2018. In 2016, 8.3 fb^{-1} of data was lost due to inefficiencies in the online vertex reconstruction, which affected the b-tagging algorithms used in the trigger. As a result, the total integrated luminosity collected in the years 2016, 2017, and 2018 was 24.6 fb^{-1}, 43.7 fb^{-1}, and 57.7 fb^{-1}, respectively. This amounts to a total integrated luminosity of 126 fb^{-1}. Data was only collected when the beam was in a stable condition and all relevant detector systems of ATLAS were deemed functional.

The primary focus of this section is to provide an overview of the analysis methods, such as the definition of signal regions and the estimation of background, in order to provide sufficient experimental context for understanding the HL-LHC extrapolations. Therefore, some details regarding the Run 2 analysis, such as its results, will not be discussed here.

Two main triggers are utilized in this analysis. They focus on the number of jets and their b-tagging status [44]. The first trigger used to select the $4b$ events for the analysis requires at least two b-tagged jets and one other additional jet ($2b1j$)[11], while the second trigger also requires at least two b-tagged jets but differs in that it needs two other additional jets ($2b2j$). The triggers also differ in their minimum transverse energy (E_T) requirement. The $2b2j$ trigger requires a 35 GeV for all its jets, while the $2b1j$ trigger

[11] The requirement for a minimum of three jets is only at the trigger level, using trigger-level jets. After the trigger, these events typically have more jets reconstructed using offline jet reconstruction algorithms. If the event still only has three jets, it will be vetoed, as outlined in selection cut 2, as shown in Figure 5.2.

requires 35 GeV for its two b-tagged jets and $100-150\,\text{GeV}$ (depending on the year of data taking) for the additional jet. Reconstruction of the jets is done via the anti-k_t algorithm [45] with a radius parameter of $R = 0.4$. The b-tagging done at the trigger level has a tagging efficiency between $40-70\%$. The MV2c20 algorithm was used in 2016, while the MV2c10 algorithm was used in 2017 and 2018 [46].

5.2 Simulated Samples

Signal events were modeled using Monte Carlo (MC) simulations. The background events, however, were modeled using a fully data-driven method outlined in section 5.5. This is because the dominant background of QCD multi-jets is difficult to simulate via MC techniques. However, to validate the data-driven background estimate, limited MC samples consisting of di-jets and $t\bar{t}$ events were used. Owing to the large number of signal variations used in the analysis, it was not practical to fully simulate a sample for each variation in κ_λ, κ_{2V}, and κ_V. For ggF initiated processes, only $\kappa_\lambda = 1$ and $\kappa_\lambda = 10$ were fully simulated. $\kappa_\lambda = 0$ and $\kappa_\lambda = 20$ were also simulated, but only at truth level, which means the detector was not simulated. For VBF, only $(\kappa_\lambda, \kappa_{2V}, \kappa_V) = (1, 1, 1)$ (SM), $(1, 1.5, 1), (2, 1, 1), (10, 1, 1), (1, 1, 0.5), (-5, 1, 0.5)$ were fully simulated. It can be theoretically shown that any signal variation of $(\kappa_\lambda, \kappa_{2V}, \kappa_V)$ can be produced using a linear combination and/or reweighting of pre-existing simulated signal samples mentioned above. This method was cross-checked with various validation samples and was found to be in agreement.

The ggF events were generated using POWHEG BOX V2[47, 48] at Next-to-Leading Order (NLO) using full NLO corrections with finite top mass and the PDF4LHC PDF set [49]. They were then normalized using the Next-to-Next-to-Leading Order (N2LO) cross-section calculated with approximate top-quark mass effects [50]. VBF events were generated at Leading-Order (LO) using MADGRAPH5_AMC@NLO [51] also with the PDF4LHC PDF set. They were then normalized to the Next-to-Next-to-Next-to-Leading Order (N3LO) cross-section [52].

In both the ggF and VBF events, PYTHIA8 was used for parton showering and hadronization [53]. Additional samples were also created using HERWIG7 [54] to assess parton shower uncertainties in using different generators. After events are processed via PYTHIA8 (or HERWIG7), they are passed through the full ATLAS detector simulation infrastructure [55]. This infrastructure uses the GEANT4 simulation tool to model the detector [55, 56].

5.3 Object and Event Reconstruction

The primary vertex is defined as the point at which a pp interaction occurs. It is reconstructed using at least two charged-particle tracks with a $p_T >$ 500 MeV measured via the ID [57]. Events may have multiple primary vertices (pile-up), but usually only one of them, known as the hard scatting primary vertex, is responsible for the interesting physics occurring in the event. The vertex with the largest sum of squared track momenta (Σp_T^2) is chosen as the hard-scatter primary vertex.

The analysis shown in this thesis hopes to measure the $HH \rightarrow b\bar{b}b\bar{b}$ process. However, neither of the Higgs bosons or any of the b quarks are directly measured. This is because the lifetime of the Higgs boson is extremely short and the b quarks undergo a process called hadronization as mentioned in section 2.3. Thus, as illustrated in figure 5.1, what is seen from the $HH \rightarrow b\bar{b}b\bar{b}$ process is neither the Higgs nor the b quarks but the resulting particles from the hadronization of the b quarks.

There are a large number of particles produced during hadronization, both electrically charged and neutral objects. Since all these particles travel in a similar direction, they form a collective cone of particles referred to as a "jet" (also illustrated in figure 5.1). Determining the properties of the original quark that produced the jet is difficult and requires dedicated algorithms.

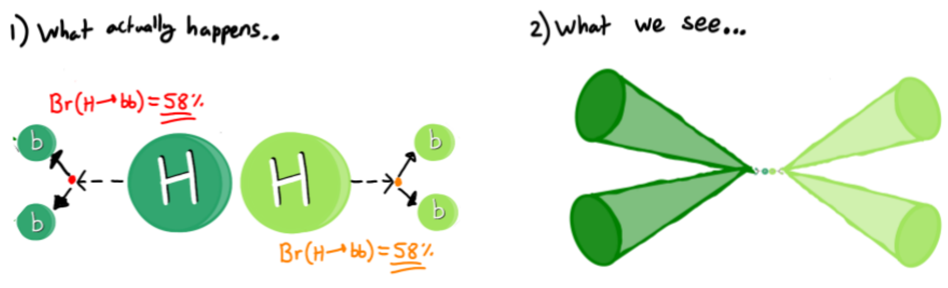

Figure 5.1: An illustration of how only the neither the Higgs or the b quarks from the $HH \rightarrow b\bar{b}b\bar{b}$ process are visible but only the resulting jets from the hadronization of the quarks.

The work of this thesis relies on the reconstruction of hadronic jets using the anti-k_t algorithm [45] with a radius parameter $R = 0.4$. In this analysis the algorithm takes particle flow objects as inputs [58].

Particle flow objects are charged jet constituents that are found to originate from the hard-scatter primary vertex. They leave behind a trail of hits in the ID, forming tracks and energy deposits in the calorimeter. These calorimeter deposits are grouped together into objects called "topological clusters". Pairing the information from the two sub-detectors is quite complementary. For example, the ID has better resolution at lower energies while the calorimeter has it better at higher energies. The ID has better angular resolution but the calorimeter has more coverage in the forward parts of the detector. And lastly, since tracks in the ID are associated with vertices, one is able to filter out tracks originating from pile-up. The particle flow algorithm [58] improves the measurement accuracy of charged-hadrons while still keeping the calorimeter measurements of neutral-particles energies. This is done by removing any double counting of charged-hadron calorimeter energy deposits by comparing their energies from the ID. Pile-up is further suppressed by using the "jet vertex tagger" (JVT) algorithm [46]. This algorithm is able to identify and reject jets that have too much of their energy originating from pile-up interactions.

Initially, jets are reconstructed at the energy scale relative to the calorimeter energy deposits, not the energy scale of the original particles that constitute the jet themselves. To overcome this, the jets are calibrated to the correct particle energy scale using a jet energy scale correction (JES) [59]. This JES correction is done via simulated MC samples, so an additional calibration is needed to correct the difference between jet energies in data and simulation [59].

The process of b-tagging is the identification of b-jets, which are jets containing b-hadrons that originate from a b-quark. The results of this thesis depend heavily on the success of b-tagging, particularly since the final state of the analysis and extrapolations includes four b quarks. Without b-tagging, every b-jet would be accompanied by $\sim$300 background jets that aren't from b-quarks, significantly lowering the sensitivity of the analysis [60]. The ATLAS collaboration uses several b-tagging algorithms to help identify b-jets, and the $HH \rightarrow b\bar{b}b\bar{b}$ analysis presented in this thesis uses the $DL1r$ algorithm [46]. These b-tagging algorithms take advantage of the relatively long lifetime of b-hadrons. The b-hadrons travel a significant distance within the detector before decaying, forming a distinct secondary vertex away from the primary hard scattering vertex. The $DL1r$ algorithm is a multi-variant classification approach that utilizes this presence of a displaced secondary vertex. It also uses other information like transverse momentum and impact parameters of ID tracks and the flight paths of b- and c- hadrons related to the suspected b-jet.

5.4 Selection and Categorization

After triggering and reconstruction (1), a series of dedicated selections numbered (2-9) are shown in figure 5.2 and are used to define regions enriched in ggF and VBF signal events. The first further selection cut (2) requires events to contain four or more central jets, where central jets are defined as $|\eta| < 2.5$ and $p_T > 40$ GeV, while forward jets have $2.5 < |\eta| < 4.5$ and $p_T > 30$ GeV. The next selection cut (3) is to require at least four of these central jets to be b-tagged. After step (3), the four highest p_T b-tagged jets

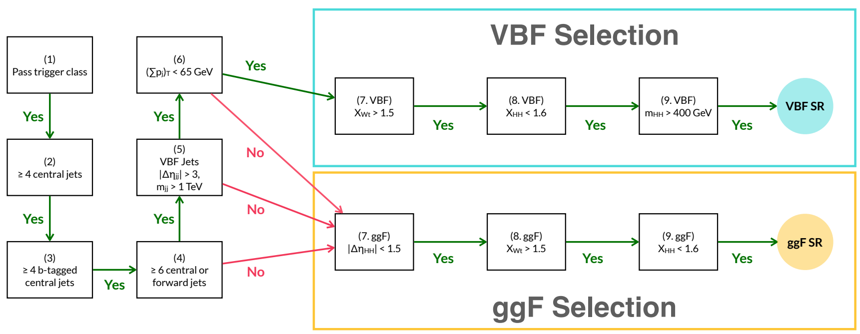

Figure 5.2: Flowchart summarizing the signal region selections of the Run 2 $HH \to b\bar{b}b\bar{b}$ analysis [19].

are chosen to reconstruct the pair of decaying Higgs bosons. Amongst these four b-tagged jets, there are three possible combinatorial pairings to form the two Higgs candidates (HC's). This is illustrated in figure 5.3. For each of the three combinatorial configurations, the pair with the largest p_T is deemed the leading HC for that configuration. The algorithm then chooses the configuration where the leading HC has the lowest ΔR. The quantity ΔR is the angular distance between the two jets that make up a pair, defined as $\Delta R = \sqrt{\Delta\eta^2 + \Delta\phi^2}$. This configuration is chosen because the pair of jets coming from a true Higgs should be more energetic and collimated due to the Higgs initial momentum, thus they should have a smaller ΔR.

It is important to not only understand how the pairing algorithm correctly pairs jets in signal events, but also to understand how it pairs jets that are not related to a Higgs bosons in background events. It is expected for background events to reach the signal region, but it is the distribution of these background events amongst the signal events that is important. Another pairing strategy could increase its efficiency by using the fact that pairs should have an invariant mass around the Higgs mass at 125 GeV.

However, this would mean that background events with no Higgs would also have reconstructed pairs with invariant masses around the Higgs mass. This would shift the background distribution to look more like the signal, and ultimately decrease sensitivity overall. After the pairs have been chosen and

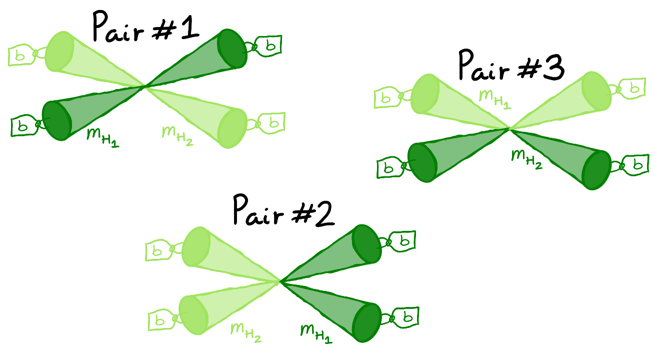

Figure 5.3: The three possible combinatorical pairings when trying to form the two two Higgs candidates (HC's) from the four highest p_T b-tagged jets.

the HC's have been reconstructed, the next step is to separate the events into two distinct categories: ggF and VBF signal regions. This is done to minimize overlap and increase sensitivity when the two regions are eventually combined. To separate the events, three cuts are applied (4, 5, 6). These cuts target the characteristic VBF event topology, which produces at least two additional energetic jets compared to ggF, due to the two outgoing quarks that first radiated the vector bosons. The first VBF cut (4) requires six or more jets, which now includes forward jets as well, to better account for the two outgoing VBF jets that are typically more longitudinally separated. The jets with the largest invariant mass (m_{jj}) are chosen as the "VBF jets".

The next VBF cut (5) requires $m_{jj} > 1$ TeV and $|\eta_{jj}| > 3$ for the VBF jets. This targets the fact that the VBF jets are expected to be energetic and well separated. The final VBF cut (6) is that the transverse component of the vector sum of momenta $(\sum p)_T$ of the two VBF jets and the four jets that make up the two HC's must be less than 65 GeV. This cut ensures that the six jets that make up the VBF system are balanced, which means the vector sum of their momenta $(\sum p)_T$ is close to 0. This is because the initial pp collision had no transverse momentum, thus any system with a large transverse momentum is unlikely to be a VBF event.

The next part of the event selection process is divided into two streams:

one for VBF events, and the other for ggF events. Each stream will use a set of final cuts that are specifically designed for the respective production mode in order to more effectively identify the signal and reduce background noise. If an event successfully passes all three VBF cuts (4, 5, 6), it will move on to the VBF stream of final cuts. If it fails any of those cuts, it will be directed to the ggF stream.

The first dedicated cut for the ggF stream (7.ggF) is to require a maximum separation in the pseudorapidity between the two HCs, $|\Delta\eta_{HH}| < 1.5$. This cut is designed to reduce the number of multi-jet background events that have separated topologies, while keeping the reduction of the signal manageable. This cut is effective because the Higgs bosons produced through the ggF process are not typically expected to have highly separated topologies. Conversely this cut is not applied for the VBF stream as many VBF events have separated topologies.

The next cut (8.ggF, 7.VBF) applies to both the ggF and VBF streams. Its purpose is to reduce background from hadronic $t\bar{t}$ decays. This cut uses a discriminant called X_{Wt}. It quantifies the likelihood that an event contains a top quark decaying into a b-quark and a W boson, which is the top quark's dominant decay process. To do this, the cut first reconstructs the W boson for each possible pairing of the central jets. Then, it pairs the reconstructed W candidate with any remaining b-tagged HC jets to form the top quark candidate. Finally, it uses the reconstructed W and top t candidates to calculate the X_{Wt} discriminant, which is defined as:

$$X_{Wt} = \min\sqrt{\left(\frac{m_W - 80.4\,\mathrm{GeV}}{0.1\ m_W}\right)^2 + \left(\frac{m_t - 172.5\,\mathrm{GeV}}{0.1\ m_t}\right)^2} \tag{5.1}$$

The reconstructed masses of the W and t candidates are represented by m_W and m_t, respectively. The cut requires $X_{Wt} > 1.5$ since a higher value of X_{Wt} indicates a lower probability that the event came from a top quark decay.

With all preliminary cuts applied, it is useful to create a 2D mass plane that plots the reconstructed mass of the leading HC (m_{H1}) against the subleading HC (m_{H2}). Figure 5.4 shows the 2D mass plane. The red lines define the analysis signal region (SR), and the dotted and dashed lines define the control regions (CR). The CR regions are used to estimate the background, as outlined in section 5.5. This 2D mass plane is useful for defining the events that make it to the SR because signal events are expected to peak around the Higgs mass with:

$$(m_{H1}, m_{H2}) \approx (125\ \mathrm{GeV}, 125\ \mathrm{GeV}) \tag{5.2}$$

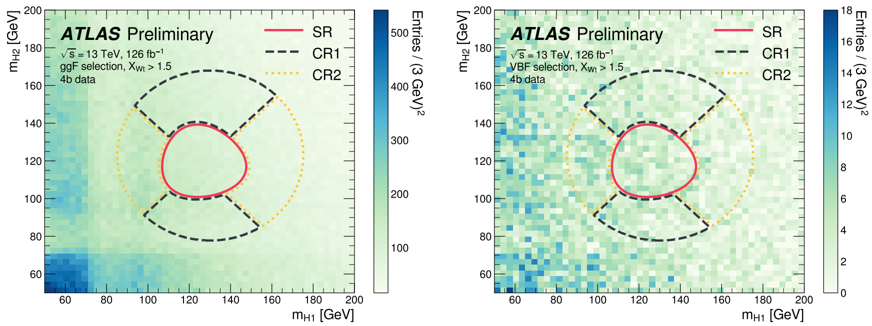

(a) ggF 4b data (b) VBF 4b data

Figure 5.4: The 4b mass planes of the reconstructed Higgs bosons candidates for the (a) ggF and (b) VBF signal selections [19].

The final shared cut (8.VBF, 9.ggF) takes advantage of this and uses a discriminant, X_{HH}, which calculates the difference between the expected signal HC masses and the actual HC masses observed for a given event. Mathematically, X_{HH} can be expressed as the following:

$$X_{HH} = \sqrt{\left(\frac{m_{H1} - 124\ GeV}{0.1\ m_{H1}}\right)^2 + \left(\frac{m_{H2} - 117\ GeV}{0.1\ m_{H2}}\right)^2} \tag{5.3}$$

where 124 GeV and 117 GeV are the expected masses for the leading HC and sub-leading HC respectively. Both of these masses are lower than the true Higgs mass of 125 GeV due to expected losses in energy from the reconstruction process. This cut requires $X_{HH} < 1.6$, where a lower value of X_{HH} indicates the event is more likely to have originated from a true HH decay. An extra final cut is applied to VBF events that have a $m_{HH} > 400$ GeV because events with lower m_{HH} were found to have poor background modeling and were removed.

5.5 Background Estimate

5.5.1 Background Estimate Method

There are two main sources of background events: QCD multi-jets, which make up 80% (90%) for ggF (VBF), and the remaining background, which is made up of $t\bar{t}$ events. One of the major improvements in comparison to the last iteration of the analysis is the new fully data-driven background estimate for both the QCD multi-jets and the $t\bar{t}$ contributions.

The technique involves using an alternative set of events which pass all the same requirements outlined in section 5.4, but with one key difference: the events have to contain exactly two b-tagged jets. These are referred to as the "2b" events, while the events that pass the normal requirements outlined in section 5.4 will be referred to as the "4b" events. Since the number of 2b events is roughly two orders of magnitude higher than the 4b events, the presence of $HH \to b\bar{b}b\bar{b}$ is negligible, and it can be safely assumed that these events are almost entirely QCD or $t\bar{t}$ background contributions. Figure 5.5 shows the 2b background mass planes for the (a) ggF and (b) VBF signal selections [19]. The background estimate takes advantage of the

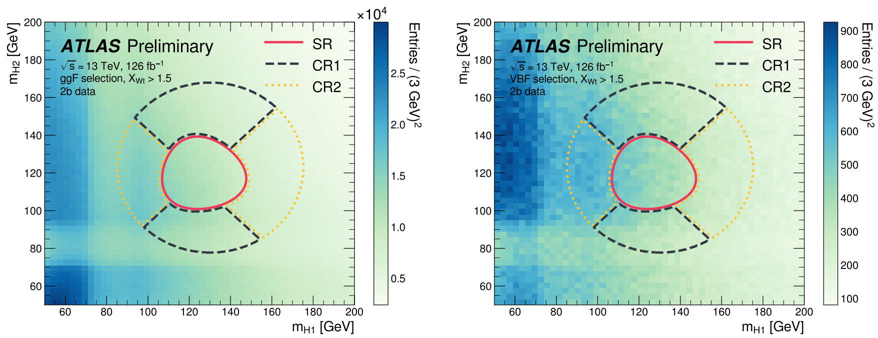

(a) ggF 2b data

(b) VBF 2b data

Figure 5.5: The 2b background mass planes of the reconstructed Higgs bosons candidates for the (a) ggF and (b) VBF signal selections [19].

consistent differences in the kinematics of 2b and 4b events across different regions of the 2D mass plane. This is done using neural networks, which learn the mapping between the kinematic distributions of 2b and 4b events in control regions CR1 and CR2. Then, by using the neural networks trained on the CR1 regions, the kinematic distributions of 2b events in the SR can be mapped onto the 4b events SR to produce the nominal background estimate.

5.5.2 Background Estimate Systematics

Additionally, one more background estimate is derived from the CR2 regions, which is used to create the **CR12 shape** systematic. This aims to quantify the arbitrary choice of using one control region over another to derive the background estimate. The systematic is defined as the difference between the CR1 and CR2 predictions in the signal region. Another important systematic is the **Bootstrap** systematic, which is designed to measure the statistical uncertainty in the background estimate. This is done by using not just one neural network, but 100 different networks for each control region. Each network is trained on a different Poisson-sampled subset of the data, known as a bootstrap sample. The background estimate is the average of the 100 different bootstrap predictions, and the bootstrap systematic is the standard deviation of those predictions.

5.6 Statistical Framework and Interpretation of Results

The statistical framework of the analysis relies on performing various maximum likelihood fits to binned m_{HH} distributions using events from the signal region. The likelihood function represents a model that predicts the data, and its inputs are parameters that can change the model's predictions. The likelihood output provides a measure of how well the model describes the data, and a better fit between the model and the data leads to a higher likelihood value. During likelihood fitting, the aim is to determine the parameter values that produce the best match between the model and the data. In a simple case with one channel and no uncertainties, the likelihood function is a product of Poisson distributions for each bin [61]. In each bin b, the Poisson distribution depends on the expected number of events, ν_b. If there is only one signal and one background source, the expected number of events in each bin can be expressed as $\nu_b = \mu\nu_b^{sig} + \nu_b^{bkg}$. In this expression, ν_b^{sig} and ν_b^{bkg} are the expected number of signal and background events, respectively, and μ represents the signal strength. The signal strength is the parameter of interest being measured by fitting the data. Given the binned distribution $n = \{n_1 ... n_b\}$, the likelihood can be expressed as:

$$\mathcal{L}(n|\mu) = \prod_{b \in \text{bins}} \text{Pois}\left(n_b|\mu\nu_b^{sig} + \nu_b^{bkg}\right) \tag{5.4}$$

5.6.1 Uncertainties

The uncertainties being considered include those related to the combined integrated luminosity, jet energy scale and resolution, and flavor tagging for b, c, and light jets. Additionally, theoretical uncertainties such as those related to parton showering, the Higgs boson cross-section, PDFs, branching fractions, and α_S are also being considered. Lastly, there is also the dominant uncertainty which comes from the data-driven background estimate.

In order to incorporate uncertainties into the likelihood, additional parameters must be added. These parameters can affect the distribution of the model used to fit the data in various ways. One way in which the parameters can affect the distribution is by changing the normalization, which alters the distribution in each bin by the same amount without changing its overall shape. Examples of normalization parameters include the signal strength μ and the parameter corresponding to the uncertainty on the total integrated luminosity. The parameters can also affect the model's distribution on a bin-by-bin basis. For example, this includes parameters that account for statistical uncertainties and those arising from the bootstrap systematic.

Nuisance parameters are parameters associated with uncertainties. Unlike the signal strength parameter μ, the nuisance parameters are not of direct interest to be measured but are still needed to help fit the model to the data. During the fit, nuisance parameters are not free to vary and are instead subject to constraints from auxiliary data. This auxiliary data, a_θ, is prior knowledge and measurements of the systematic associated with the parameter θ. A probability distribution is used by the likelihood function to encode each constraint. In this analysis, a Gaussian distribution is typically employed[12], which specifies a nominal expected value of the parameter and an associated width that represents the uncertainty. When adding in the nuisance parameters and constraint terms, denoted by θ and c_θ respectively, the likelihood becomes:

$$\mathcal{L}(n|\mu,\theta) = \prod_{b\in\text{bins}} \text{Pois}\left(n_b|\nu_b(\mu,\theta)\right) \quad \prod_{\theta\in\boldsymbol{\theta}} c_\theta(a_\theta|\theta) \tag{5.5}$$

5.6.2 Statistical Tests

For the Standard Model signal hypothesis and different values of κ_λ and κ_{2V}, upper limits are set on the signal strength μ and the signal cross-sections, following the CLs prescription [62]. Fixing the signal strength $\mu = 1$, the likelihood function can be parametrized by κ_λ and κ_{2V}, allowing for likelihood scans to be produced with respect to these coupling modifiers. The expected discovery significance, which is the rejection of the background-only $\mu = 0$ hypothesis, is also calculated. Unlike setting limits, the discovery significance is (to first order) independent of the signal model. The statistical analysis done in this work relied heavily on the use of two software implementations: pure-Python HistFactory (pyhf) [63, 64] and quickstats [65].

[12]The constraint function to use depends on the auxiliary measurement, Poisson constraints and log-normal constraints are also commonly used [61]

Chapter 6

Extrapolation to HL-LHC

6.1 Integrated Luminosity and Center of Mass Energy at HL-LHC

To account for differences in experimental conditions between Run 2 and the HL-LHC, a set of multiplicative factors, known as scale factors, are applied to the signal and background distributions of the Run 2 analysis. In the case of Run 2, all scale factors have a value of one. The most significant scale factor affecting the signal and background distributions is due to the expected increase in luminosity for the HL-LHC. This scale factor is defined as the ratio between the target HL-LHC integrated luminosity of 3000 fb^{-1} and the Run 2 integrated luminosity of 126 fb^{-1}.

Another scale factor is applied to take into account the increase in center-of-mass energy from $\sqrt{s} = 13$ TeV to $\sqrt{s} = 14$ TeV. For the ggF and VBF HH signals, these scale factors are 1.18 and 1.19 respectively [66]. This increase in energy will also result in an increase in the multi-jet background, which is estimated to be scaled by a factor of 1.18 as was done in the previous projection [21]. The effects of pile-up have not been studied directly in this work. A simplifying assumption has been made that any decrease in sensitivity caused by pile-up is balanced by improvements in the detector, trigger, and reconstruction. This assumption is backed by studies examining the conditions at the HL-LHC [67].

6.2 Systematic Scenarios

Additional scale factors are introduced to quantify the potential changes in the systematic uncertainties from Run 2 to the HL-LHC. A scale factor of one indicates that the systematic uncertainty is the same size as in the Run 2 analysis. The systematic scale factors used here for the HL-LHC are equal to or less than one, implying that no uncertainty will increase relative to their Run 2 size. This is due to anticipated improvements in the detectors, theoretical predictions, and analysis techniques.

To explore the impact of systematic uncertainties, various scenarios are evaluated using different sets of systematic scale factors. Four main scenarios, as detailed below, are used, following a similar approach as for the $b\bar{b}\gamma\gamma$ and $b\bar{b}\tau\bar{\tau}$ projections in [68, 69]:

- (No syst. unc.) A scenario considering only statistical uncertainties to demonstrate the effects of completely removing all experimental uncertainties. In this scenario, all systematic scale factors are set to zero.

- (Baseline) A baseline scenario where relevant systematic uncertainties are scaled down, following the improvements expected with the larger HL-LHC dataset available [70]. The data-driven background uncertainties are also reduced according to the integrated luminosity. This consists in a 50% reduction of the bootstrap uncertainty at the HL-LHC, while the shape uncertainty is assumed to be identical to Run 2. Table 6.1 shows a summary of the considered uncertainty scale factors in this scenario.

- (Theoretical unc. halved) A scenario where Run 2 experimental uncertainties are considered and theoretical uncertainties associated with HH signals are halved, imagining a situation where theoretical methods improve but experimental methods remain unchanged compared to the conditions at the HL-LHC.

- (Run 2 syst. unc) A scenario where uncertainties are maintained at the same level as in Run 2, representing the most challenging scenario where neither theoretical nor experimental techniques show improvement compared to the conditions at the HL-LHC.

Section 7.4 explores additional systematic scenarios by examining the impact of data-driven background uncertainties in greater detail.

Table 6.1: Summary of the systematic uncertainty scale factors considered in the HL-LHC baseline scenario. A scale factor of one indicates that the systematic uncertainty is the same size as in the Run 2 analysis. The considered systematic uncertainties include: theoretical; flavour-tagging; jets; luminosity; and the data-driven background bootstrap and shape uncertainties.

Systematic uncertainties	Scale factors for HL-LHC baseline scenario
Theoretical uncertainty	0.5
b-jet tagging efficiency	0.5
c-jet tagging efficiency	0.5
Light-jet tagging efficiency	1.0
Jet energy scale and resolution	1.0
Luminosity	0.6
Background bootstrap uncertainty	0.5
Background shape uncertainty	1.0

Chapter 7

Results

7.1 HH signal strength

Table 7.1 shows the 95% CL upper limit on the SM HH signal strength μ, as well as the expected discovery significance, calculated with respect to the background-only hypothesis and combining the ggF and VBF channels, for the various systematic uncertainty scenarios outlined in Section 6. For the baseline systematic uncertainty scenario a significance of 1.0σ is expected, while for the scenario without systematic uncertainties this value increases to 1.8σ.

The results from the previous $HH \to b\bar{b}b\bar{b}$ projections [21, 22] reported a 95% CL upper limit on the signal strength of 3.5 (1.5) and a significance of 0.6σ (1.4σ).[13] These updated results improve the upper limits on the HH signal strength and the discovery significance by $40 - 65\%$ when comparing the baseline scenario to the previous projection performed with Run 2 systematic uncertainties. Figure 7.1 shows the 95% CL upper limit on the

[13] The previous $HH \to b\bar{b}b\bar{b}$ result and hence prospect studies did not include the large theoretical uncertainty originating from the scheme and scale choice of the virtual top-quark mass [71]. Additionally, the previous projection did not consider any bootstrap systematic uncertainty since the partial Run 2 version of the $b\bar{b}b\bar{b}$ search did not account for such a systematic uncertainty.

Table 7.1: Projected HL-LHC 95% CL upper limits on the $HH \to b\bar{b}b\bar{b}$ production signal strength and discovery significance.

Uncertainty scenario	Signal strength 95% CL upper limit	Discovery significance [σ]
No syst. unc.	1.1	1.8
Baseline	2.0	1.0
Theoretical unc. halved	3.1	0.6
Run 2 syst. unc.	3.4	0.6

HH signal strength and the discovery significance for values of integrated luminosity ranging from 1000 fb^{-1} to 3000 fb^{-1}.

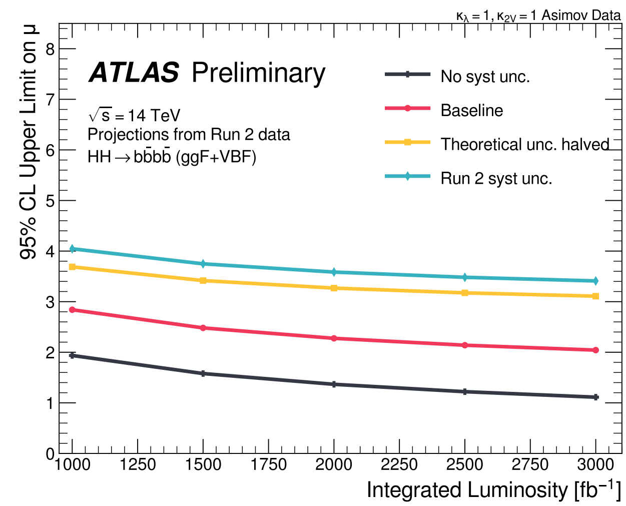

(a) 95% CL upper limit

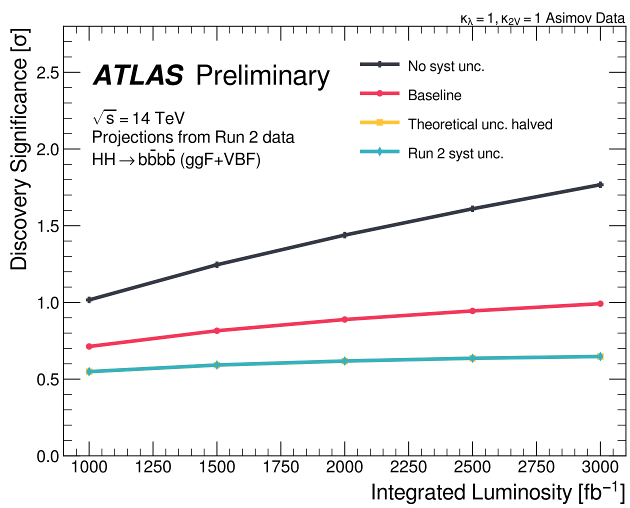

(b) Discovery significance

Figure 7.1: The 95% CL upper limits (a) on the signal strength and discovery significance (b) evaluated at various integrated luminosity values ranging from 1000 fb^{-1} to 3000 fb^{-1}. The significances of the scenarios associated to Run 2 systematic uncertainties and halved values of theoretical uncertainties are perfectly overlaid.

7.2 Constraints on κ_λ

Confidence intervals (CI) on κ_λ are derived by scanning the negative log-likelihood function at different values of κ_λ with an Asimov background-plus-signal dataset assumed under the SM signal hypothesis ($\kappa_\lambda = 1$). The crossing of the likelihood scan with the values of 1 and 3.84 correspond to the 68% (1σ) and 95% CI of the κ_λ parameter. Figure 7.2a illustrates the results from the likelihood scans in the four systematic uncertainty scenarios previously introduced. On top of the main minimum at $\kappa_\lambda = 1$, a secondary minimum can be observed at κ_λ values around 5. This results from a reduced acceptance of the $HH \to b\bar{b}b\bar{b}$ analysis in these BSM scenarios that, combined with the higher theoretical HH cross-section, results in a similar event yield to the SM HH signal. The 68% and 95% CI for κ_λ are reported in Table 7.2.

Under the HL-LHC baseline scenario, the 68% CI for κ_λ is found at $[-0.5, 6.1]$. This CI is estimated to be $[0.1, 2.6]$ without systematic uncertainties. In contrast, the κ_λ 68% CI of the previous $b\bar{b}b\bar{b}$ projections were estimated to be $[-2.3, 6.4]$ ($[-0.4, 4.3]$) with (without) systematic uncertainties. This projection shows a general improvement, mainly due to the updates on the analysis strategy, data-driven background estimation, and b-jet tagging performance. It can be noted that the halved theoretical uncertainty scenario is very close to the scenario with Run 2 systematic uncertainties. This implies that theoretical uncertainties of HH signals have a negligible impact if compared to other systematic uncertainties. As it will be discussed later in Section 7.4, the sensitivity of the $b\bar{b}b\bar{b}$ channel to HH signals is dominated by the data-driven background uncertainties, while the other experimental uncertainties are found to play a sub-leading role.

The discovery significance was also calculated for a range of κ_λ values

Table 7.2: A summary of the κ_λ constraints for various HL-LHC systematic uncertainty scenarios. The 68% and 95% CI are extracted from a likelihood scan of κ_λ assuming $\kappa_\lambda = 1$ as signal hypothesis in the Asimov dataset.

Uncertainty scenario	κ_λ 68% CI	κ_λ 95% CI
No syst. unc.	[0.1, 2.6]	[-0.5, 6.4]
Baseline	[-0.5, 6.1]	[-1.6, 7.5]
Theoretical unc. halved	[-1.2, 6.9]	[-2.6, 8.5]
Run 2 syst. unc.	[-1.2, 6.9]	[-2.8, 8.5]

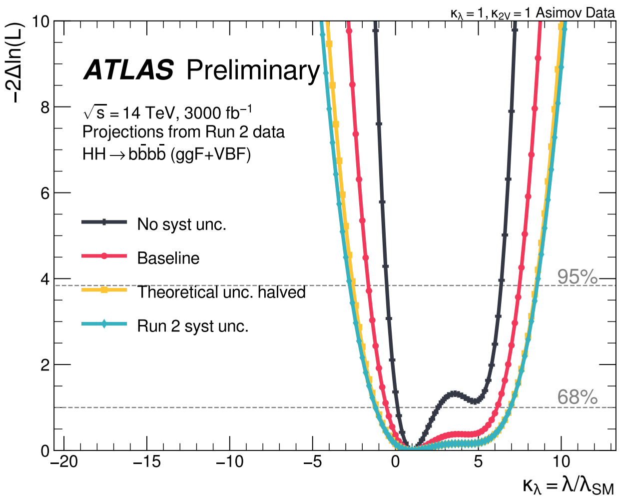

(a) κ_λ likelihood scan

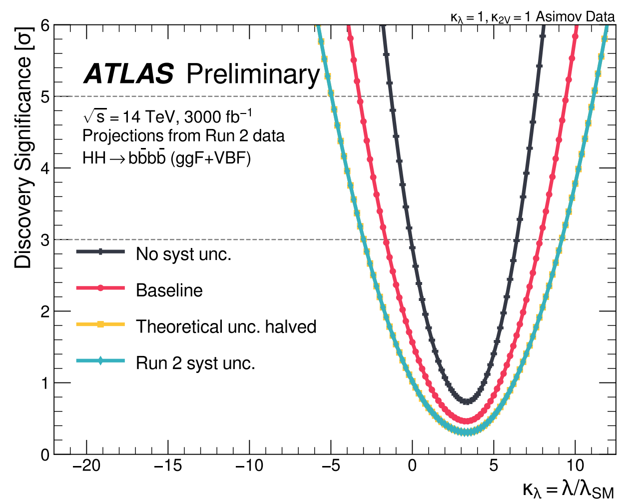

(b) Discovery significance vs κ_λ

Figure 7.2: Profile likelihood scans (a) and discovery significance (b) evaluated at different values of the κ_λ coupling modifier in the resolved Run 2 $HH \to b\bar{b}b\bar{b}$ analysis for various HL-LHC systematic uncertainty scenarios. In (a) the scans are derived considering a $\kappa_\lambda = 1$ Asimov dataset, and the intersections of the dashed horizontal lines with the profile likelihood curve define the 68% and 95% confidence intervals, respectively. In b) dashed horizontal lines correspond to $3\,\sigma$ and $5\,\sigma$ significance.

and the resulting scan is reported in 7.2b.

As well as assuming the SM scenario of $\kappa_\lambda = 1$, a likelihood scan was also performed under the $\kappa_\lambda = 0$ hypothesis and can be seen in figure 7.3. These results reveal a higher sensitivity to the $\kappa_\lambda = 0$ hypothesis compared to the SM hypothesis, as expected due to its larger predicted cross-section[14]. The scan shows that the analysis is more sensitive to the $\kappa_\lambda = 0$ hypothesis over the SM hypothesis, which is expected since the prior has a larger predicted cross section.

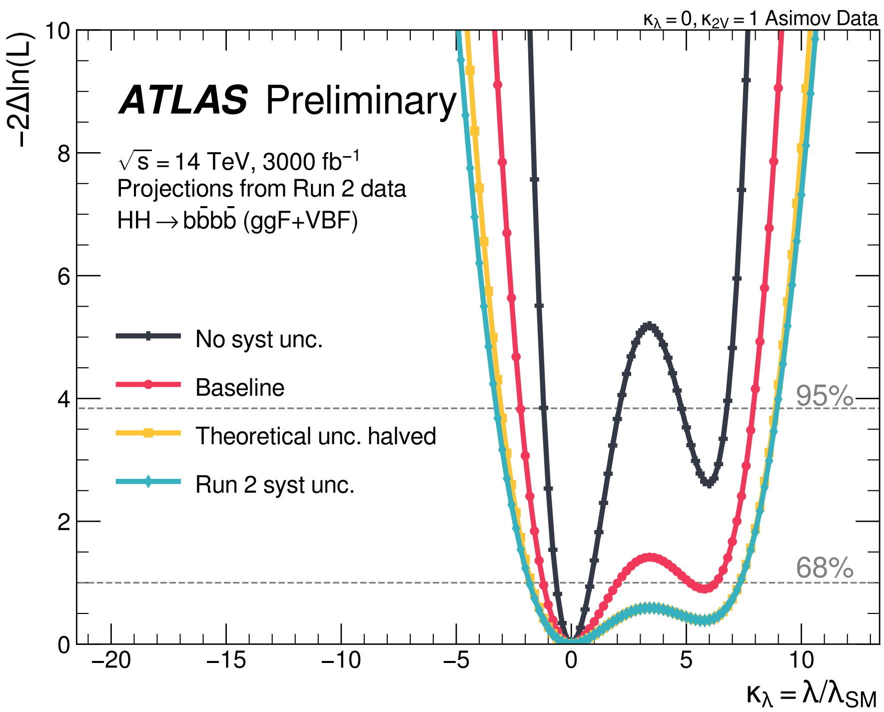

Figure 7.3: The κ_λ likelihood scan for non-SM $\kappa_\lambda = 0$ Asimov data, for various HL-LHC systematic uncertainty scenarios. The intersections of the dashed horizontal lines with the profile likelihood curve define the 68% and 95% confidence intervals, respectively.

[14]The total ggF + VBF predicted cross-section as a function of κ_λ is shown using the red curve in figure A.1

7.3 Constraints on κ_{2V}

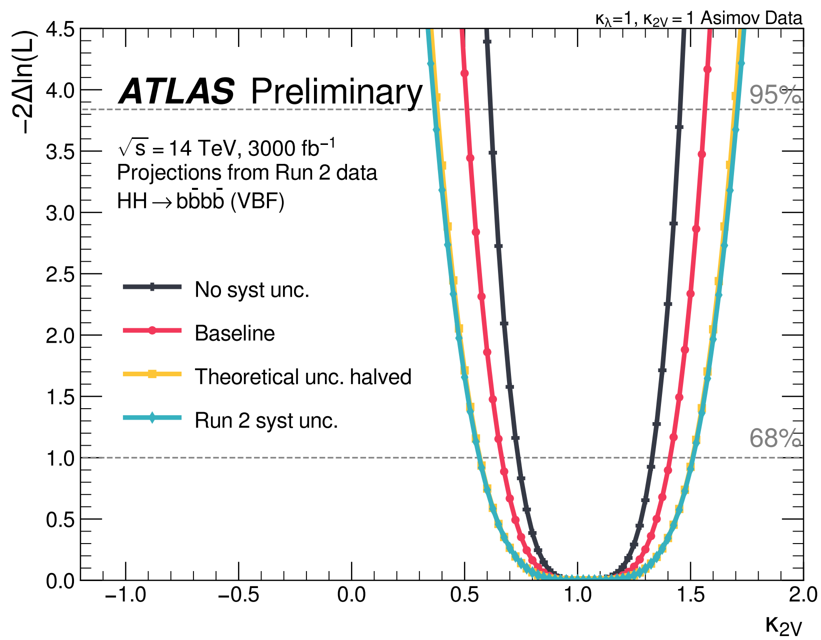

Figure 7.4: Profile likelihood scan evaluated at different values of the κ_{2V} $HHVV$ coupling modifier in the resolved Run 2 $HH \to b\bar{b}b\bar{b}$ analysis for various HL-LHC systematic uncertainty scenarios. The scans are derived considering a $\kappa_\lambda = 1$ and $\kappa_{2V} = 1$ Asimov dataset. The intersections of the dashed horizontal lines with the profile likelihood curve define the 68% and 95% confidence intervals, respectively.

A likelihood scan for the $HHVV$ coupling modifier κ_{2V} is also performed following an identical procedure to the κ_λ likelihood scan. Figure 7.4 shows the results of the scan for different systematic uncertainty scenarios assuming $\kappa_{2V} = 1$ and $\kappa_\lambda = 1$ as signal hypothesis in the Asimov dataset. Under the HL-LHC baseline scenario, the 68% CI for κ_{2V} is found to be $[0.7, 1.4]$, while when systematic uncertainties are ignored the 68% constraints reduce to $[0.7, 1.3]$. The 68% and 95% CI for κ_{2V} in the different systematic uncertainty scenarios are reported in Table 7.3.

7.4 Impact of the data-driven background systematic uncertainties

Systematics uncertainties related to the data-driven background estimate are found to be the dominant uncertainties in this updated $HH \to b\bar{b}b\bar{b}$ projection. Further studies of these systematic uncertainties are documented in this section. To explore the potential impact of reducing the background shape and bootstrap systematic uncertainties at the HL-LHC, several dedicated data-driven background systematic uncertainty scenarios are defined. In the future, the bootstrap uncertainty could be reduced from the enhanced statistic of the dataset used for the training of the data-driven background estimation, while the shape systematic could be improved through more sophisticated background estimation methods. A summary of the considered scenarios and their scaling factors can be found in Table 7.4. Other systematic uncertainties than the data-driven background ones are fixed to the baseline values indicated in Table 6.1. Scaling factors of 0.2 are chosen here for the improved scenarios since the decrease in the statistical uncertainty from 126 fb^{-1} to 3000 fb^{-1} is around 0.2, providing a good benchmark for potential improvement in the systematic uncertainties.

The κ_λ likelihood curve assuming $\kappa_\lambda = 1$ signal is displayed in figure 7.5. The 95% CL upper limits on the signal strength, the discovery significance and the 68% CI from the likelihood scan are summarized in Table 7.5.

Table 7.3: A summary of the κ_{2V} constraints for various HL-LHC systematic uncertainty scenarios. The 68% and 95% CI are extracted from a likelihood scan of κ_{2V} assuming $\kappa_{2V} = 1$ as signal hypothesis in the Asimov dataset.

Uncertainty scenario	68% CI	95% CI
No syst. unc.	[0.7, 1.3]	[0.6, 1.5]
Baseline	[0.7, 1.4]	[0.5, 1.6]
Theoretical unc. halved	[0.6, 1.5]	[0.4, 1.7]
Run 2 syst. unc.	[0.6, 1.5]	[0.4, 1.7]

Table 7.4: Summary of the dedicated background systematic uncertainty scenarios and their scaling factors. Other systematic uncertainties are fixed to the baseline values indicated in Table 6.1.

	Scaling factors (sf)	
Uncertainty scenario	Bootstrap unc.	Shape unc.
Pessimistic bkg. unc.	1.0	1.0
Conservative bkg. unc. 1 (fix bootstrap unc.)	1.0	0.2
Conservative bkg. unc. 2 (fix shape unc.)	0.2	1.0
Optimistic bkg. unc.	0.2	0.2

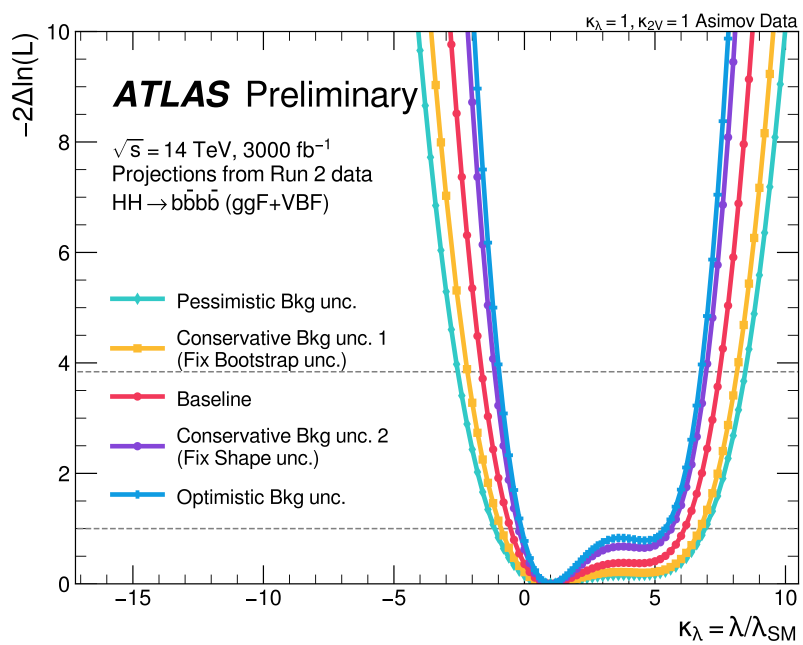

Figure 7.5: The profile likelihood scans for the κ_λ coupling modifier for the dedicated background scenarios (and the baseline scenario for comparison) using an Asimov dataset with $\kappa_\lambda = 1$. The intersections of the dashed horizontal lines with the profile likelihood curve define the 68% and 95% confidence intervals, respectively.

Table 7.5: Results summary for the 95% CL upper limit on the signal strength, the discovery significance and the 68% CI from the likelihood scan for the dedicated background systematic uncertainty scenarios.

Uncertainty scenario	Signal strength 95% CL upper limit	Discovery significance [σ]	κ_λ 68% CI
Pessimistic bkg. unc.	3.1	0.6	[-1.1, 6.9]
Conservative bkg. unc. 1	2.7	0.7	[-0.9, 6.7]
Conservative bkg. unc. 2	1.6	1.3	[-0.2, 5.6]
Optimistic bkg. unc.	1.4	1.4	[-0.1, 5.4]

7.5 Further study of systematics

Comparing various uncertainty scenarios with the pessimistic one shows that the bootstrap uncertainty has the greatest impact on sensitivity. Meanwhile, the shape uncertainty has a smaller effect. This can be seen in figure 7.6, which shows the discovery significance and 95% CL upper limits when one systematic uncertainty is varied and the others are kept constant. The dominance of the bootstrap systematic uncertainty over the shape systematic uncertainty is expected because the shape uncertainty is constrained by the fit, reducing its impact. The bootstrap systematic uncertainty is less constrained because it is more uncorrelated across the m_{HH} spectrum, leading to a greater effect on the projection results when its improved[15].

The dominance of the background bootstrap and shape systematics can be seen further in figure 7.7. This figure shows a heat map representing the percentage loss in the upper limit of the signal strength μ when an individual systematic (on the x-axis) is removed for a given systematic scenario (on the y-axis). The first row of 7.7 shows the results from the blinded Run 2 analysis[19] with 126 fb^{-1}. The theoretical systematics are dominant in this scenario, reducing the upper limit by 11%. The bootstrap and shape systematics reduce the upper limit by 10% and 6.5%, respectively. The theoretical systematics are largely unaffected by the number of events. For instance, the uncertainty in the branching ratio of $H \to b\bar{b}$ remains at 3.4% in both scenarios with Run 2 sized systematics, regardless of the luminosity. While the bootstrap and shape systematics are dependent on the number of events and sensitive to the shape of the m_{HH} distribution, their impact increases dramatically when the HL-LHC luminosity is introduced into the Run 2 scenario.

7.5.1 Bootstrap systematic

The impact of the bootstrap systematic is highest in the "HL-LHC lumi & Run 2 syst unc." and "Pessimistic Bkg ubc." scenarios. This is because the absolute size of the bootstrap systematic uncertainty is largest in these two scenarios along with the "Conservative bkg. unc. 1 (fix bootstrap unc.)" scenario. In the latter case, the effect of removing the bootstrap systematic is slightly less than in the other two prior mentioned scenarios, as the upper limit is already lower due to the smaller size of the other systematics. Studies

[15] The shape is split into four kinematic regions per category (there are 6 categories in total for ggF, and 2 for VBF), one nuisance parameter (NP) each, while the bootstrap has a NP per bin, hence it is more uncorrelated.

from the Run 2 analysis show that the bootstrap systematic will decrease with the increased number of events at the HL-LHC[16]. Nevertheless, given the significant impact of the bootstrap systematic on sensitivity, alternative methods should be considered in the future, with a focus on developing background models that are not so heavily dependent on the 4b control region.

7.5.2 Shape systematic

The impact of the shape systematic is highest in the "Conservative bkg. unc. 2 (fix shape unc.)", "HL-LHC lumi & Run 2 syst unc." and "Pessimistic Bkg ubc." scenarios[17]. This is because the shape systematic is at its maximum in these scenarios. However, the Bootstrap systematic is still at its maximum size too in the latter two mentioned scenarios, which prevents a greater decrease in the limit. The results indicate that the current method of estimating uncertainty is not adequate for the HL-LHC. To address this, it may be necessary to have more flexibility in the shape systematic. This could be achieved by dividing the uncertainty into more than the four kinematic regions currently used, introducing more NPs and less constraint.

7.5.3 Ranking plots

The "Pessimistic Bkg unc." scenario, in which background systematics are the largest, reveals the significant difference in the constraints of the shape and bootstrap systematics during the fit. This can be seen in the ranking plot shown in figure 7.8. The y-axis displays the 10 NPs with the greatest impact, while the x-axis shows the change in the size of each NP's constraint from their pre-fit error bars (in red) to the post-fit error bars (in black). Figure 7.8a shows that the shape systematic NPs become more constrained after fitting, while figure 7.8b shows a relatively constant constraint for the bootstrap NPs. This explains why shape systematics have less impact on the limits when they are removed, as shown in Figure 7.7. For more information on the constraints of the shape and bootstrap systematics using different systematic scenarios, see Appendix C.

[16] This is shown by the Run 2 3b1f validation region [19]

[17] As well as the Theoretical unc. halved scenario but that is pretty much identical to the "HL-LHC lumi & Run 2 syst unc." when it comes to the behavior of the bkg systs since it only has the theory systs different

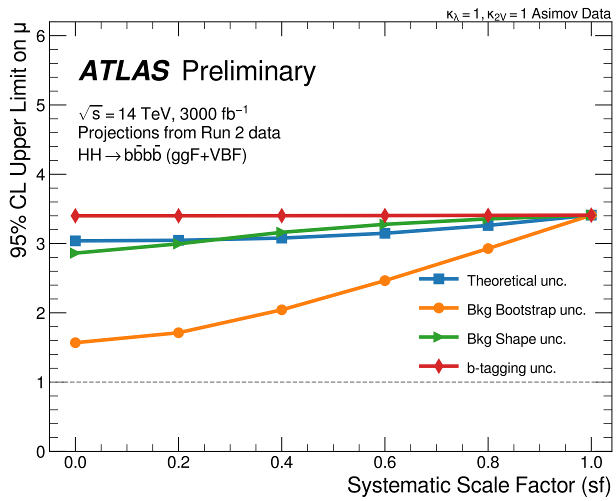

(a) 95% CL upper limit on μ

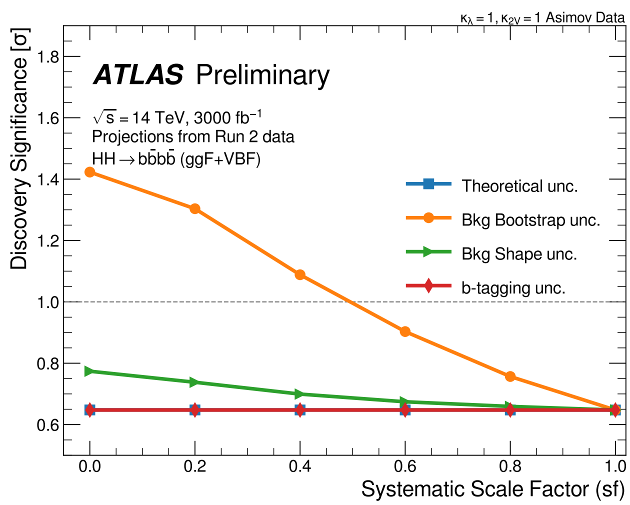

(b) Discovery significance

Figure 7.6: The 95% CL upper limits (a) on the HH signal strength and discovery significance (b) evaluated for a range of scale factors for theoretical signal uncertainties, b-tagging uncertainties, and the background bootstrap and shape uncertainties. The scale factors range from 0 to 1, where 1 corresponds to the uncertainty being unchanged with respect to their Run 2 values and 0 neglect the systematic uncertainty. For each point, only the systematic uncertainty of interest is changed while other uncertainties are kept unchanged.

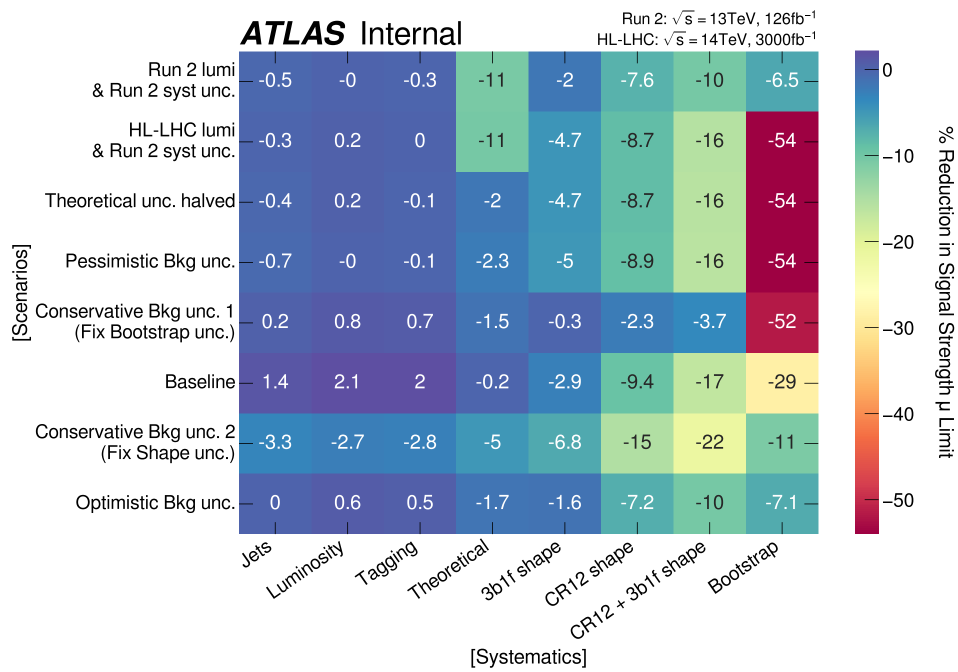

Figure 7.7: A heat-map representing the percentage % loss in the upper limit of the signal strength μ for a given systematic scenario (y-axis) when an individual systematic (x-axis) is removed. Results from the blinded Run 2 analysis with 126 fb^{-1} are included for comparison in the first row, while the second row is Run 2 systematics but with HL-LHC luminosity at 3000 fb^{-1} ("Run 2 sys. unc.").

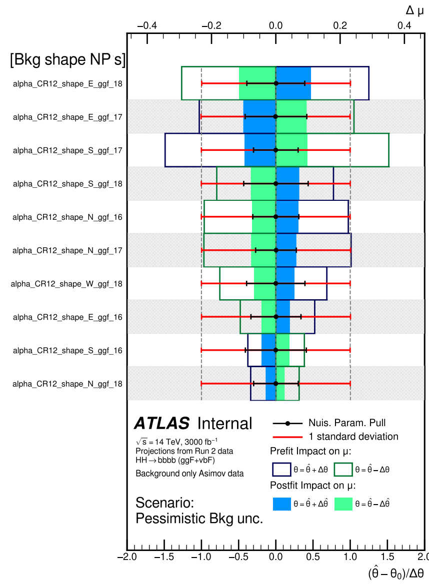

(a) Shape systematic

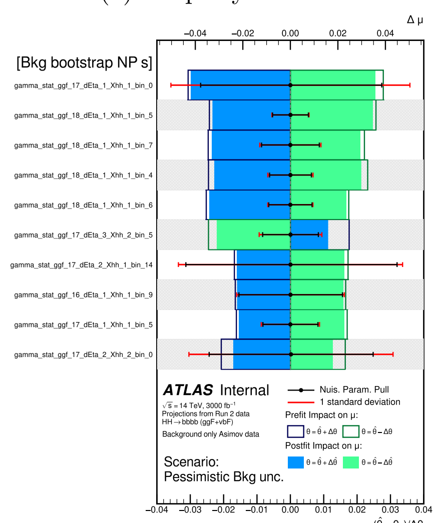

(b) Bootstrap systematic

Figure 7.8: The constraints of the shape (a) and bootstrap (b) systematics using the "Pessimistic Bkg unc." scenario.

7.6 Impact of the b-tagging efficiency

The impact of the b-tagging efficiency on the 95% CL upper limit on the signal strength and the discovery significance is shown in figure 7.9. These results, based on an approach similar to the one employed in Ref. [72], are obtained by applying a scale factor which accounts for the truth flavour composition of signals and backgrounds. The scale factor calculation assumes constant light-flavour-jet rejection while the b-tagging efficiency is varied. The truth-flavour composition of the QCD multi-jet background is extracted from di-jet simulation, and approximately 65% of the simulated events are found to be composed of events with four true b-initiated jets. The rest of the QCD multijet background is due to events entering the analysis SR through mis-identification of true light- and c-initiated jets as reconstructed b-jets. Using a 85% b-tagging efficiency working point, a discovery significance of 1.1σ could be achieved, corresponding to an improvement of approximately 10% with respect to the 77% b-tagging efficiency working point currently exploited by the Run 2 analysis. When systematic uncertainties are ignored, this value increase to 2.2σ.

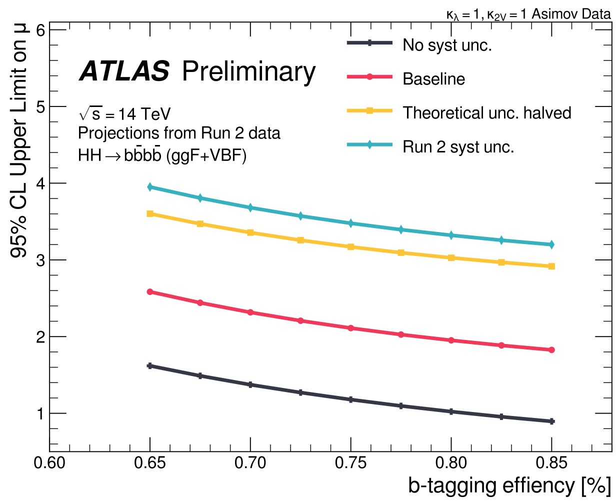

(a) 95% CL upper limit on μ

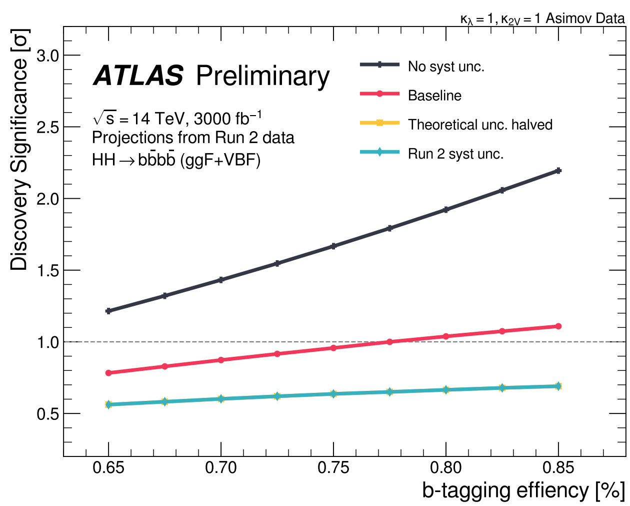

(b) Discovery significance

Figure 7.9: The 95% CL upper limits (a) on the HH signal strength and discovery significance (b) evaluated for a range of b-tagging efficiency values from 65% to 85% assuming the light-jet rejection rate as the 77% working point used in Run 2.

Chapter 8

Conclusion

An updated projection of the $HH \to b\bar{b}b\bar{b}$ analysis at the HL-LHC is presented. The projection uses the latest $HH \to b\bar{b}b\bar{b}$ result, based on 126 fb^{-1} of data collected with the ATLAS detector during the Run 2 of the LHC. Under the background-only hypothesis, the 95% CL upper limit on the HH signal strength is found to be 2.0 times the Standard Model prediction and the discovery significance 1.0σ in a baseline systematic uncertainty scenario, where relevant systematic uncertainties are scaled down while the rest are left unchanged with respect to the Run 2 result. Constraints on the coupling modifiers κ_λ and κ_{2V} are also presented, where 68% CI are set at $[-0.5, 6.1]$ for κ_λ and $[0.7, 1.4]$ for κ_{2V} in the baseline systematic uncertainty scenario. The impact of theoretical HH uncertainties is found to be negligible in the $b\bar{b}b\bar{b}$ channel, and the dominant source of systematic uncertainty is the bootstrap uncertainty of the data-driven background estimation. Compared to the previous $HH \to b\bar{b}b\bar{b}$ extrapolations based on the partial Run 2 data-set, this result is improved thanks to the improved analysis strategy and b-jet identification obtained at the end of Run 2. As new analysis techniques continue to rapidly develop, it is possible that these projections will be shown to be pessimistic when the HL-LHC era arrives. HH is expected to be near the discovery threshold at the HL-LHC, and the $b\bar{b}b\bar{b}$ channel, the most common final state, along with the two most sensitive channels, $b\bar{b}\gamma\gamma$ and $b\bar{b}\tau\tau$, will be critical in any HH discovery.

Bibliography

[1] The ATLAS Collaboration. "Observation of a new particle in the search for the Standard Model Higgs boson with the ATLAS detector at the LHC". In: *Physics Letters B* 716.1 (Sept. 2012), pp. 1–29. DOI: 10.1016/j.physletb.2012.08.020. URL: https://doi.org/10.1016%2Fj.physletb.2012.08.020.

[2] The CMS Collaboration. "Observation of a new boson at a mass of 125 GeV with the CMS experiment at the LHC". In: *Physics Letters B* 716.1 (Sept. 2012), pp. 30–61. DOI: 10.1016/j.physletb.2012.08.021. URL: https://doi.org/10.1016%2Fj.physletb.2012.08.021.

[3] The ATLAS Collaboration. "Study of the spin and parity of the Higgs boson in diboson decays with the ATLAS detector". In: *The European Physical Journal C* 75.10 (Oct. 2015). DOI: 10.1140/epjc/s10052-015-3685-1. URL: https://doi.org/10.1140%2Fepjc%2Fs10052-015-3685-1.

[4] The CMS Collaboration. "Constraints on the spin-parity and couplings of the Higgs boson in proton collisions at 7 and 8 TeV". In: *Physical Review D* 92.1 (July 2015). DOI: 10.1103/physrevd.92.012004. URL: https://doi.org/10.1103%2Fphysrevd.92.012004.

[5] The ATLAS Collaboration. "A combination of measurements of Higgs boson production and decay using up to 139 fb^{-1} of proton–proton collision data at $\sqrt{s} = 13$ TeV collected with the ATLAS experiment". In: (2020). URL: https://cds.cern.ch/record/2725733.

[6] The CMS Collaboration. "Combined Higgs boson production and decay measurements with up to 137 fb-1 of proton-proton collision data at sqrts = 13 TeV". In: (2020). URL: https://cds.cern.ch/record/2706103.

[7] R. L. Workman et al. "Review of Particle Physics". In: *PTEP* 2022 (2022), p. 083C01. DOI: 10.1093/ptep/ptac097.

[8] Rick S. Gupta. "BSM Theories Face Higgs Coupling data". In: (2013). DOI: 10.48550/ARXIV.1311.3040. URL: https://arxiv.org/abs/1311.3040.

[9] Giuseppe Degrassi et al. "Higgs mass and vacuum stability in the Standard Model at NNLO". In: *Journal of High Energy Physics* 2012.8 (Aug. 2012). DOI: 10.1007/jhep08(2012)098. URL: https://doi.org/10.1007%2Fjhep08%282012%29098.

[10] Valerio De Luca, Alex Kehagias, and Antonio Riotto. "On the cosmological stability of the Higgs instability". In: *Journal of Cosmology and Astroparticle Physics* 2022.09 (Sept. 2022), p. 055. DOI: 10.1088/1475-7516/2022/09/055. URL: https://doi.org/10.1088%2F1475-7516%2F2022%2F09%2F055.

[11] Sebastian Bruggisser et al. "Electroweak Phase Transition and Baryogenesis in Composite Higgs Models". In: (2018). DOI: 10.48550/ARXIV.1804.07314. URL: https://arxiv.org/abs/1804.07314.

[12] James M Cline and Kimmo Kainulainen. "Electroweak baryogenesis and dark matter from a singlet Higgs". In: *Journal of Cosmology and Astroparticle Physics* 2013.01 (Jan. 2013), pp. 012–012. DOI: 10.1088/1475-7516/2013/01/012. URL: https://doi.org/10.1088%2F1475-7516%2F2013%2F01%2F012.

[13] Biagio Di Micco et al. "Higgs boson potential at colliders: Status and perspectives". In: *Reviews in Physics* 5 (2020), p. 100045. ISSN: 2405-4283. DOI: https://doi.org/10.1016/j.revip.2020.100045. URL: https://www.sciencedirect.com/science/article/pii/S2405428320300083.

[14] Ding Yu Shao et al. "Threshold resummation effects in Higgs boson pair production at the LHC". In: *Journal of High Energy Physics* 2013.7 (July 2013). DOI: 10.1007/jhep07(2013)169. URL: https://doi.org/10.1007%2Fjhep07%282013%29169.

[15] Daniel de Florian and Javier Mazzitelli. "Higgs pair production at next-to-next-to-leading logarithmic accuracy at the LHC". In: (2015). DOI: 10.48550/ARXIV.1505.07122. URL: https://arxiv.org/abs/1505.07122.

[16] J. Baglio et al. "$gg \to HH$: Combined uncertainties". In: *Phys. Rev. D* 103 (5 Mar. 2021), p. 056002. DOI: 10.1103/PhysRevD.103.056002. URL: https://link.aps.org/doi/10.1103/PhysRevD.103.056002.

[17] The ATLAS Collaboration. "Constraining the Higgs boson self-coupling from single- and double-Higgs production with the ATLAS detector using pp collisions at $\sqrt{s} = 13$ TeV". In: (2022). URL: https://cds.cern.ch/record/2816332.

[18] Rafael Teixeira De Lima. "Accessing HH at ATLAS and CMS with the HL-LHC". In: *PoS* LHCP2020 (2021), p. 082. DOI: 10.22323/1.382.0082. URL: https://cds.cern.ch/record/2779642.

[19] The ATLAS Collaboration. "Search for non-resonant pair production of Higgs bosons in the $b\bar{b}b\bar{b}$ final state in pp collisions at $\sqrt{s} = 13$ TeV with the ATLAS detector". In: (2022). URL: http://cds.cern.ch/record/2811390/.

[20] The ATLAS Collaboration. "Search for pair production of Higgs bosons in the $b\bar{b}b\bar{b}$ final state using proton-proton collisions at $\sqrt{s} = 13$ TeV with the ATLAS detector". In: *JHEP* 1901 (2019), p. 030. DOI: 10.1007/JHEP01(2019)030. arXiv: 1804.06174. URL: https://cds.cern.ch/record/2313703.

[21] The ATLAS Collaboration. "Projected sensitivity to non-resonant Higgs boson pair production in the $b\bar{b}b\bar{b}$ final state using proton–proton collisions at HL-LHC with the ATLAS detector". In: (2016). URL: https://cds.cern.ch/record/2221658.

[22] The ATLAS Collaboration. "Measurement prospects of the pair production and self-coupling of the Higgs boson with the ATLAS experiment at the HL-LHC". In: (2018). URL: https://cds.cern.ch/record/2652727.

[23] Flournoy, Alex. "PHGN 423 Particle Physics". In: (2019). URL: https://inside.mines.edu/~aflourno/Particle/423.shtml.

[24] Hauser, Rainer. "Introduction to the standard model of particle physics part 1". In: (2019). URL: https://www.rainerhauser.ch/public/scripts/StandardModel1.pdf.

[25] David Galbraith. "UX: Standard model of the standard model". In: *david galbraith* (Dec. 2013). URL: http://davidgalbraith.org/portfolio/ux-standard-model-of-the-standard-model/.

[26] De Angelis, Matthew. "Gauge Theories". In: (2015). URL: https://users.hep.manchester.ac.uk/u/dasgupta/teaching/PHYS-40682/Gauge-Theories-lecture-notes-by-Matthew-De-Angelis.pdf.

[27] C Csáki and P Tanedo. "Beyond the Standard Model". en. In: (2015). DOI: 10.5170/CERN-2015-004.169. URL: http://cds.cern.ch/record/2119546.

[28] A. Pomarol. "Beyond the Standard Model". In: (2012). DOI: 10.48550/ARXIV.1202.1391. URL: https://arxiv.org/abs/1202.1391.

[29] Hitoshi Murayama. "Physics Beyond the Standard Model and Dark Matter". In: (2007). DOI: 10.48550/ARXIV.0704.2276. URL: https://arxiv.org/abs/0704.2276.

[30] A. D. Sakharov. "Violation of CP Invariance, C asymmetry, and baryon asymmetry of the universe". In: *Pisma Zh. Eksp. Teor. Fiz.* 5 (1967), pp. 32–35. DOI: 10.1070/PU1991v034n05ABEH002497.

[31] Andreas Papaefstathiou, Simon Plätzer, and Kazuki Sakurai. "On the phenomenology of sphaleron-induced processes at the LHC and beyond". In: *Journal of High Energy Physics* 2019.12 (Dec. 2019). DOI: 10.1007/jhep12(2019)017. URL: https://doi.org/10.1007%2Fjhep12%282019%29017.

[32] Dan Hooper and Gordan Krnjaic. "GUT baryogenesis with primordial black holes". In: *Physical Review D* 103.4 (Feb. 2021). ISSN: 2470-0010. DOI: 10.1103/PhysRevD.103.043504. URL: https://www.osti.gov/biblio/1763855.

[33] Yuval Grossman, Yosef Nir, and Riccardo Rattazzi. "CP Violation Beyond the Standard Model". In: (June 1998), pp. 755–794. DOI: 10.1142/9789812812667_0011. URL: https://doi.org/10.1142%2F9789812812667_0011.

[34] A. Giarnetti. "BSM sources of CP violation at future long baseline experiments". In: *Journal of Physics: Conference Series* 2156.1 (Dec. 2021), p. 012179. DOI: 10.1088/1742-6596/2156/1/012179. URL: https://dx.doi.org/10.1088/1742-6596/2156/1/012179.

[35] Manuel Reichert et al. "Probing baryogenesis through the Higgs boson self-coupling". In: *Phys. Rev. D* 97.7 (2018), p. 075008. DOI: 10.1103/PhysRevD.97.075008. arXiv: 1711.00019 [hep-ph].

[36] Ewa Lopienska. "The CERN accelerator complex, layout in 2022. Complexe des accélérateurs du CERN en janvier 2022". In: (2022). URL: https://cds.cern.ch/record/2800984.

[37] Riccardo Maria Bianchi and ATLAS Collaboration. "ATLAS experiment schematic illustration". In: (2022). URL: http://cds.cern.ch/record/2837191.

[38] The Atlas Collaboration. "ATLAS inner detector: Technical Design Report, 1". In: Technical design report. ATLAS (1997). URL: https://cds.cern.ch/record/331063.

[39] The Atlas Collaboration. "ATLAS calorimeter performance: Technical Design Report". In: Technical design report. ATLAS (1996). URL: http://cds.cern.ch/record/331059.

[40] The Atlas Collaboration. "ATLAS muon spectrometer: Technical Design Report". In: Technical design report. ATLAS (1997). URL: https://cds.cern.ch/record/331068.

[41] Takuya Nobe. "Triggering in ATLAS in Run 2 and Run 3". In: (2021). URL: http://cds.cern.ch/record/2773071.

[42] Tony Affolder. "ATLAS Phase II Upgrade". In: (2022). URL: https://cds.cern.ch/record/2799535.

[43] The Atlas Collaboration. "Technical Design Report for the Phase-II Upgrade of the ATLAS TDAQ System". In: (2017). DOI: 10.17181/CERN.2LBB.4IAL.

[44] The Atlas Collaboration. "Configuration and performance of the ATLAS b-jet triggers in Run 2". In: *Eur. Phys. J. C* 81.12 (2021), p. 1087. DOI: 10.1140/epjc/s10052-021-09775-5. arXiv: 2106.03584 [hep-ex].

[45] Matteo Cacciari, Gavin P. Salam, and Gregory Soyez. "The anti-kt jet clustering algorithm". In: *Journal of High Energy Physics* 2008.04 (Apr. 2008), p. 063. DOI: 10.1088/1126-6708/2008/04/063. URL: https://dx.doi.org/10.1088/1126-6708/2008/04/063.

[46] The Atlas Collaboration. "ATLAS flavour-tagging algorithms for the LHC Run 2 pp collision dataset". In: (2022). DOI: 10.48550/ARXIV.2211.16345. URL: https://arxiv.org/abs/2211.16345.

[47] Paolo Nason. "A New method for combining NLO QCD with shower Monte Carlo algorithms". In: *JHEP* 11 (2004), p. 040. DOI: 10.1088/1126-6708/2004/11/040. arXiv: hep-ph/0409146.

[48] Stefano Frixione, Paolo Nason, and Carlo Oleari. "Matching NLO QCD computations with Parton Shower simulations: the POWHEG method". In: *JHEP* 11 (2007), p. 070. DOI: 10.1088/1126-6708/2007/11/070. arXiv: 0709.2092 [hep-ph].

[49] Jon Butterworth et al. "PDF4LHC recommendations for LHC Run II". In: *Journal of Physics G: Nuclear and Particle Physics* 43.2 (Jan. 2016), p. 023001. DOI: 10.1088/0954-3899/43/2/023001. URL: https://doi.org/10.1088%2F0954-3899%2F43%2F2%2F023001.

[50] M. Grazzini et al. "Higgs boson pair production at NNLO with top quark mass effects". In: *Journal of High Energy Physics* 2018.5 (May 2018). DOI: 10.1007/jhep05(2018)059. URL: https://doi.org/10.1007%2Fjhep05%282018%29059.

[51] Johan Alwall et al. "MadGraph 5: going beyond". In: *Journal of High Energy Physics* 2011.6 (June 2011). DOI: 10.1007/jhep06(2011)128. URL: https://doi.org/10.1007%2Fjhep06%282011%29128.

[52] Frédéric A. Dreyer and Alexander Karlberg. "Vector-Boson Fusion Higgs Production at Three Loops in QCD". In: *Physical Review Letters* 117.7 (Aug. 2016). DOI: 10.1103/physrevlett.117.072001. URL: https://doi.org/10.1103%2Fphysrevlett.117.072001.

[53] Torbjörn Sjöstrand et al. "An introduction to PYTHIA 8.2". In: *Computer Physics Communications* 191 (June 2015), pp. 159–177. DOI: 10.1016/j.cpc.2015.01.024. URL: https://doi.org/10.1016%2Fj.cpc.2015.01.024.

[54] Johannes Bellm et al. "Herwig 7.0/Herwig 3.0 release note". In: *The European Physical Journal C* 76.4 (Apr. 2016). DOI: 10.1140/epjc/s10052-016-4018-8. URL: https://doi.org/10.1140%2Fepjc%2Fs10052-016-4018-8.

[55] E Ritsch. "The ATLAS Integrated Simulation Framework". In: (2013). URL: https://cds.cern.ch/record/1532476.

[56] S. Agostinelli et al. "GEANT4–a simulation toolkit". In: *Nucl. Instrum. Meth. A* 506 (2003), pp. 250–303. DOI: 10.1016/S0168-9002(03)01368-8.

[57] Federico Meloni. "Primary vertex reconstruction with the ATLAS detector". In: 12 (2016). DOI: 10.1088/1748-0221/11/12/C12060. URL: https://cds.cern.ch/record/2222390.

[58] The ATLAS Collaboration. "Jet reconstruction and performance using particle flow with the ATLAS Detector". In: *The European Physical Journal C* 77.7 (July 2017). DOI: 10.1140/epjc/s10052-017-5031-2. URL: https://doi.org/10.1140%2Fepjc%2Fs10052-017-5031-2.

[59] The ATLAS Collaboration. "Jet energy scale and resolution measured in proton–proton collisions at $\sqrt{s} = 13$ TeV with the ATLAS detector". In: *Eur. Phys. J. C* 81.8 (2021), p. 689. DOI: 10.1140/epjc/s10052-021-09402-3. arXiv: 2007.02645 [hep-ex].

[60] The Atlas Collaboration. "ATLAS flavour-tagging algorithms for the LHC Run 2 *pp* collision dataset". In: (2022). DOI: 10.48550/ARXIV.2211.16345. URL: https://arxiv.org/abs/2211.16345.

[61] Kyle Cranmer et al. "HistFactory: A tool for creating statistical models for use with RooFit and RooStats". In: (2012). URL: https://cds.cern.ch/record/1456844.

[62] A L Read. "Presentation of search results: the CLs technique". In: *Journal of Physics G: Nuclear and Particle Physics* 28.10 (Sept. 2002), p. 2693. DOI: 10.1088/0954-3899/28/10/313. URL: https://dx.doi.org/10.1088/0954-3899/28/10/313.

[63] Lukas Heinrich, Matthew Feickert, and Giordon Stark. "pyhf: v0.7.0". Version 0.7.0. In: (2022). DOI: 10.5281/zenodo.1169739. URL: https://doi.org/10.5281/zenodo.1169739.

[64] Lukas Heinrich et al. "pyhf: pure-Python implementation of HistFactory statistical models". In: *Journal of Open Source Software* 6.58 (2021), p. 2823. DOI: 10.21105/joss.02823. URL: https://doi.org/10.21105/joss.02823.

[65] Alkaid Cheng. "quickstats: A tool for quick statistical analysis for HEP experiments". In: (2022). URL: https://pypi.org/project/quickstats/.

[66] The ATLAS Collaboration. "HL-LHC prospects for the measurement of Higgs boson pair production in the $b\bar{b}b\bar{b}$ final state and combination with the $b\bar{b}\gamma\gamma$ and $b\bar{b}\tau^+\tau^-$ final states at the ATLAS experiment". In: (2022). URL: https://cds.cern.ch/record/2841244.

[67] The ATLAS and CMS collaborations. "Snowmass White Paper Contribution: Physics with the Phase-2 ATLAS and CMS Detectors". In: (2022). URL: https://cds.cern.ch/record/2805993.

[68] The ATLAS Collaboration. "Projected sensitivity of Higgs boson pair production in the $bb\tau\tau$ final state using proton-proton collisions at HL-LHC with the ATLAS detector". In: (2021). URL: https://cds.cern.ch/record/2798448.

[69] The ATLAS Collaboration. "Measurement prospects of Higgs boson pair production in the $b\bar{b}\gamma\gamma$ final state with the ATLAS experiment at the HL-LHC". In: (2022). URL: https://cds.cern.ch/record/2799146.

[70] Andrea Dainese et al. "Report on the Physics at the HL-LHC, and Perspectives for the HE-LHC". In: (2019). DOI: 10.23731/CYRM-2019-007. URL: https://cds.cern.ch/record/2703572.

[71] Joshua Davies, Florian Herren, and Matthias Steinhauser. "Top Quark Mass Effects in Higgs Boson Production at Four-Loop Order: Virtual Corrections". In: *Physical Review Letters* 124.11 (Mar. 2020). DOI: 10.1103/physrevlett.124.112002. URL: https://doi.org/10.1103%5C%2Fphysrevlett.124.112002.

[72] The Atlas Collaboration. "Expected performance of the ATLAS detector under different High-Luminosity LHC conditions". In: (2021). URL: https://cds.cern.ch/record/2776650.

[73] Wojciech Bizoń, Ulrich Haisch, and Luca Rottoli. "Constraints on the quartic Higgs self-coupling from double-Higgs production at future hadron colliders". In: *JHEP* 1910 (2019), p. 267. DOI: 10.1007/JHEP10(2019)267. arXiv: 1810.04665. URL: https://cds.cern.ch/record/2643544.

[74] Riccardo-Maria Bianchi et al. "Event visualization in ATLAS". In: 7 (2017). DOI: 10.1088/1742-6596/898/7/072014. URL: https://cds.cern.ch/record/2248396.

[75] Paul Adrien Maurice Dirac and Ralph Howard Fowler. "The quantum theory of the electron". In: *Proceedings of the Royal Society of London. Series A, Containing Papers of a Mathematical and Physical Character* 117.778 (1928), pp. 610–624. DOI: 10.1098/rspa.1928.0023. eprint: https://royalsocietypublishing.org/doi/pdf/10.1098/rspa.1928.0023. URL: https://royalsocietypublishing.org/doi/abs/10.1098/rspa.1928.0023.

[76] Sanjoy Mandal et al. "Toward deconstructing the simplest seesaw mechanism". In: *Physical Review D* 105.9 (May 2022). DOI: 10.1103/physrevd.105.095020. URL: https://doi.org/10.1103%2Fphysrevd.105.095020.

[77] M. Reichert et al. “Probing baryogenesis through the Higgs boson self-coupling”. In: *Physical Review D* 97.7 (Apr. 2018). DOI: 10.1103/physrevd.97.075008. URL: https://doi.org/10.1103%2Fphysrevd.97.075008.

[78] G Apollinari et al. “High Luminosity Large Hadron Collider HL-LHC”. en. In: (2015). DOI: 10.5170/CERN-2015-005.1. URL: https://cds.cern.ch/record/2120673.

[79] The Atlas Collaboration. “Expected *b*-tagging performance with the upgraded ATLAS Inner Tracker detector at the High-Luminosity LHC”. In: (2020). URL: http://cds.cern.ch/record/2713377.

[80] M.P. Casado. “A High-Granularity Timing Detector for the ATLAS Phase-II upgrade”. In: *Nuclear Instruments and Methods in Physics Research Section A: Accelerators, Spectrometers, Detectors and Associated Equipment* 1032 (2022), p. 166628. ISSN: 0168-9002. DOI: https://doi.org/10.1016/j.nima.2022.166628. URL: https://www.sciencedirect.com/science/article/pii/S0168900222002005.

[81] T Kawamoto et al. “New Small Wheel Technical Design Report”. In: (2013). URL: https://cds.cern.ch/record/1552862.

[82] The ATLAS Collaboration. “Performance of b-jet identification in the ATLAS experiment”. In: *Journal of Instrumentation* 11.04 (Apr. 2016), P04008–P04008. DOI: 10.1088/1748-0221/11/04/p04008. URL: https://doi.org/10.1088%2F1748-0221%2F11%2F04%2Fp04008.

[83] The ATLAS Collaboration. “Expected tracking and related performance with the updated ATLAS Inner Tracker layout at the High-Luminosity LHC”. In: (2021). URL: http://cds.cern.ch/record/2776651.

Appendices

Appendix A

Cross-section upper limit scan as function of κ_λ

The projected 95% CL upper limits on the HH cross-section as a function of κ_λ are shown in A.1 for the baseline uncertainty scenario for the $b\bar{b}b\bar{b}$ channel. The limits are derived assuming no HH production using the CLs method [62]. No theoretical uncertainties in the HH cross section calculation is considered. Indirect constraints on κ_λ can be derived from the intersection of the projection cross-section upper limit with the κ_λ-dependent theoretical prediction of the HH production cross-section at $\sqrt{s} = 14\,\text{TeV}$ [73]. The HH production is expected to be excluded at 95 % CL for values of κ_λ outside the interval $[2.1, 4.0]$ when combining all three channels. Limits for other uncertainty scenarios, and for each input channel are shown in A.1.

Table A.1: Projected κ_λ interval outside which the HH cross-section is excluded at 95% CL for different uncertainty scenarios for an integrated luminosity of 3000 fb^{-1} at $\sqrt{s} = 14\,\text{TeV}$. The limits are obtained from cross-section scans comparing different κ_λ signal hypotheses to the background-only hypothesis.

Uncertainty scenario	95 % CL limits on κ_λ from cross-section scan
No syst. unc.	$[0.8, 5.6]$
Baseline	$[-0.6, 6.8]$
Theoretical unc. halved	$[-1.7, 7.9]$
Run 2 syst. unc.	$[-1.8, 7.9]$

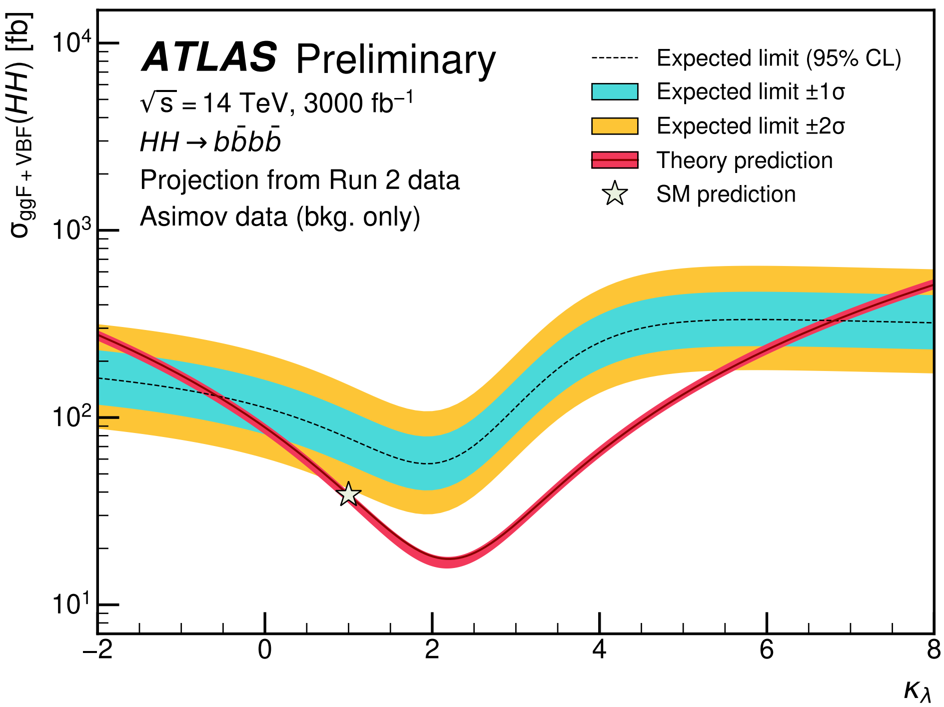

Figure A.1: Expected 95 % CL limits on the HH cross-section for different κ_λ hypotheses at $\sqrt{s} = 14\,\text{TeV}$, 3000 fb^{-1} at the HL-LHC with the baseline uncertainty scenario, for the $b\bar{b}b\bar{b}$ channel The expected cross-section limits assume a complete absence of HH production. The theory prediction curve represents the situation where all parameters and couplings are set to their SM values except for κ_λ. The SM hypothesis corresponds to $\kappa_\lambda = 1$.

Appendix B

Cross-section upper limit scan as function of κ_{2V}

The projected 95% CL upper limits on the HH cross-section as a function of κ_{2V} are shown in B.1 for the baseline uncertainty scenario for the $b\bar{b}b\bar{b}$ channel. Following a similar procedure as illustrated in Appendix A, B.1 shows the κ_{2V} intervals outside which the VBF HH cross-section is excluded at 95%CL for different systematic uncertainty scenarios for the $b\bar{b}b\bar{b}$ channel.

Table B.1: Projected interval of κ_{2V} outside which VBF HH cross-section is excluded at 95% CL for different uncertainty scenarios for an integrated luminosity of 3000 fb^{-1} at $\sqrt{s} = 14$ TeV. The limits are obtained from cross-section scans comparing different κ_{2V} signal hypotheses to the background-only hypothesis.

Uncertainty scenario	95 % CL limits on κ_{2V} from cross-section scan
No syst. unc.	[0.6, 1.5]
Baseline	[0.5, 1.6]
Theoretical unc. halved	[0.4, 1.7]
Run 2 syst. unc.	[0.4, 1.7]

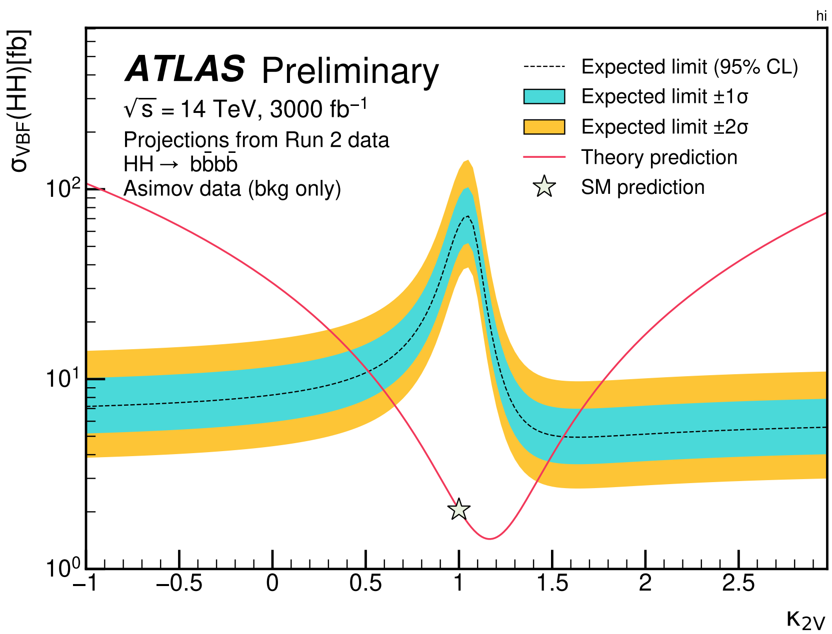

Figure B.1: Expected 95 % CL limits on the HH cross-section for different κ_{2V} hypotheses at $\sqrt{s} = 14\,\text{TeV}$, 3000 fb^{-1} at the HL-LHC with the baseline uncertainty scenario. The expected cross-section limits assume a complete absence of HH production. The theory prediction curve represents the situation where all parameters and couplings are set to their SM values except for κ_{2V}. The SM hypothesis corresponds to $\kappa_{2V} = 1$.

Appendix C

Further scenario showing constraints of the bootstrap and shape systematics

In section 7, the constraints were shown using the “Pessimistic Bkg unc.” where the background systematics are largest. Here the “Optimistic bkg. unc.” scenario is used where the background systematics are smallest and consequently the constraints are reduced since there is less reduction of the systematics since they’re already reduced. The constraints are shown in figure C.1

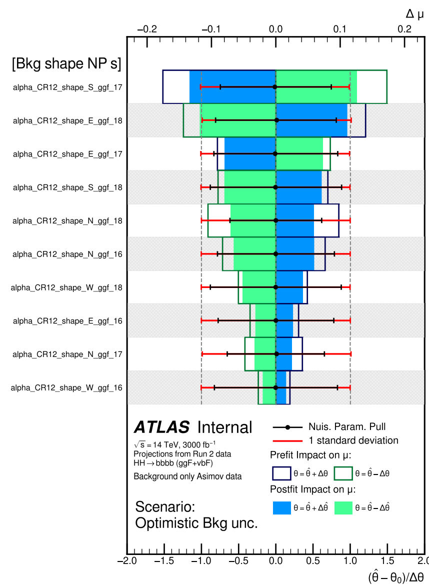

(a) Shape systematic

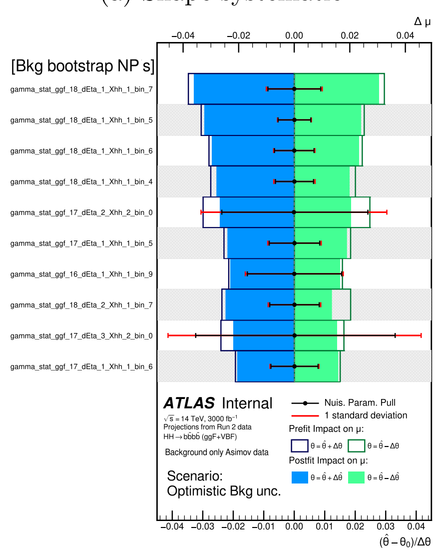

(b) Bootstrap systematic

Figure C.1: The constraints of the shape a and bootstrap b systematics using the “Optimistic bkg. unc.”.

Appendix D

Simplified illustrations for $HH \to 4b$

Various drawings to simplify and explain various stages of the $HH \to 4b$ analysis.

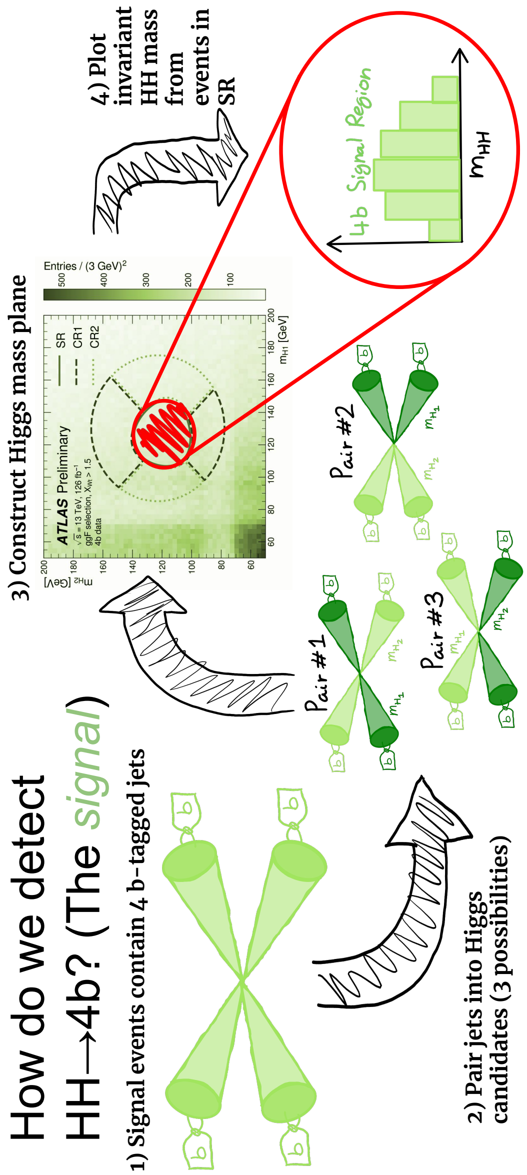

Figure D.1: Simplified illustration of how the $HH \to 4b$ obtains signal events

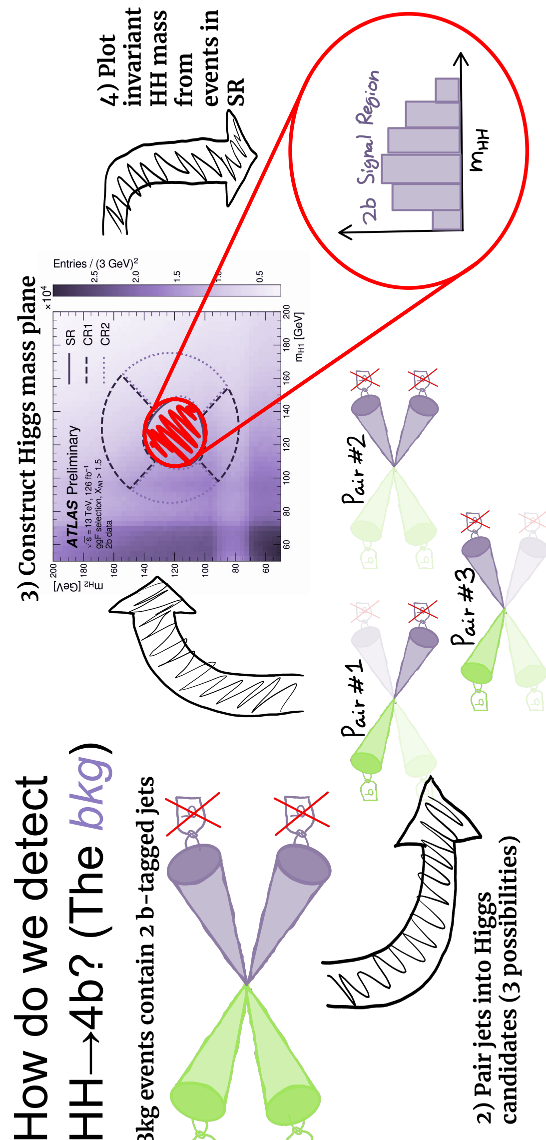

Figure D.2: Simplified illustration of how the $HH \to 4b$ obtains background events

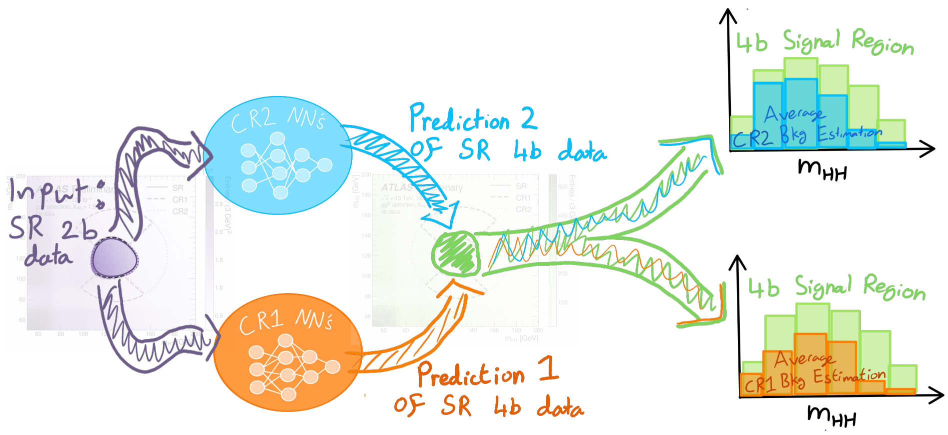

Figure D.3: Simplified illustration the $HH \to 4b$ background estimate

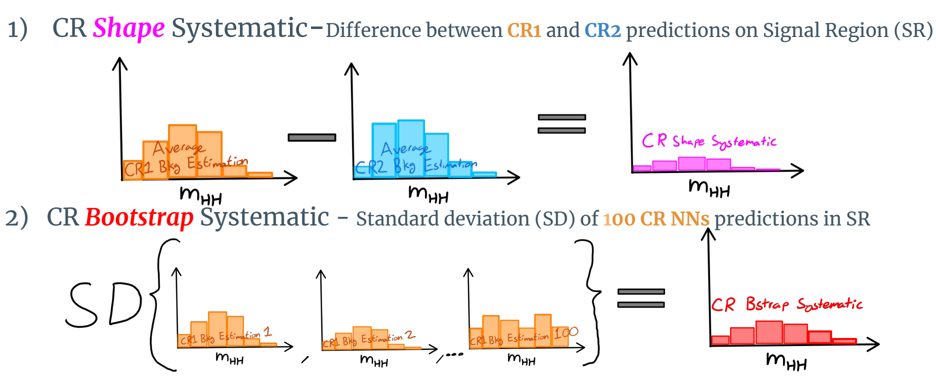

Figure D.4: Simplified illustration the $HH \to 4b$ background systematics

Appendix E

Event display for $HH \to 4b$

Event display generated using VP1[74], for the Run 2 analysis showing a prospective $HH \to 4b$ event shown in figure E.1

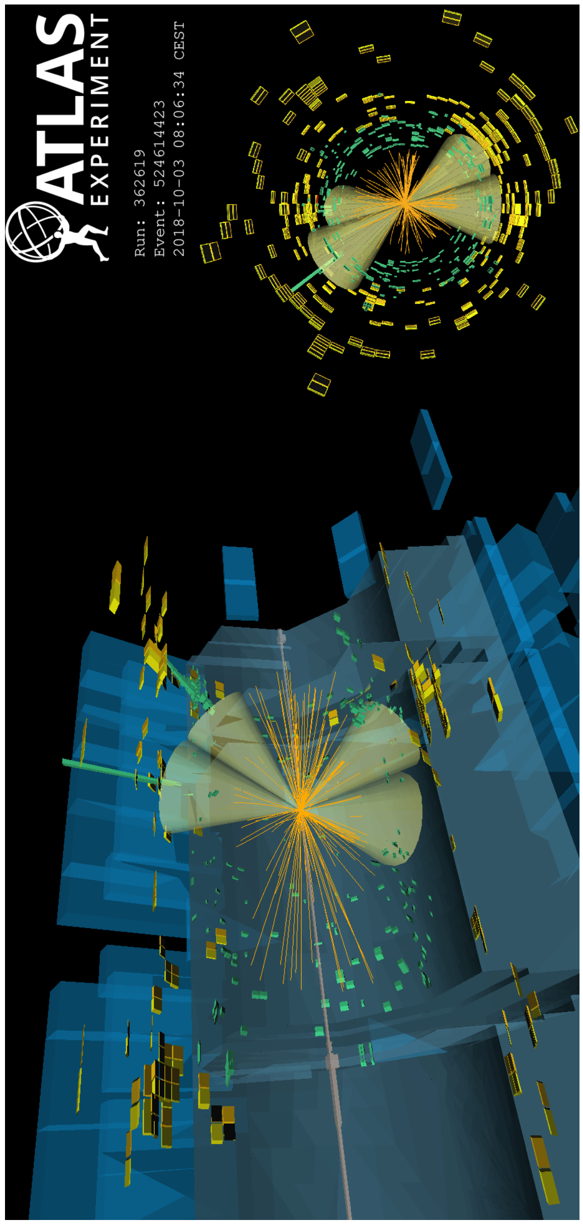

Figure E.1: Event display of a candidate $HH \rightarrow 4b$ event at the ATLAS detector

Appendix F

Dancing Cat analogy for the Instability of the Higgs Potential

Figure F.1 depicts a simplifying analogy to describe the instability of the Higgs potential. The analogy imagines the Universe as a dancing cat, where a fundamental property of this cat (universe) is that it wears a hat with a pom-pom attached to the top (shown in purple). Unfortunately, the threading that attaches the pom-pom to the hat has become undone, causing the pom-pom to be free to move about. This is problematic because if the pom-pom falls off while the cat is dancing, it would make the cat very sad, but even worse, it could also lead to the collapse of our universe as we know it. The hat of the cat represents the Higgs potential, and the different vertical positions of the pom-pom correspond to different masses for fundamental particles, such as the electron. If the pom-pom falls off while the cat is dancing, the mass of the electron and other fundamental particles would change, causing our laws of chemistry and physics to be rewritten and resulting in the collapse of our universe.

The hats in the analogy represent varying levels of stability in the Higgs potential. The red beanie hat represents an unstable universe, where the sides of the hat go straight down and cause the pom-pom to fall off easily. In contrast, the green upside-down magician's hat represents a stable universe, where the sides of the hat go straight up and prevent the pom-pom from falling off. The yellow sombrero hat represents the current shape of the Higgs potential according to theory and experimental measurements.

Figure F.1: Dancing cat analogy for the instability of the Higgs potential